Advanced Electronic Materials

ADVANCED ELECTRONIC MATERIALS Open Access

www.advelectronicmat.de

RESEARCH ARTICLE OPEN ACCESS

Effects of Doping, Disorder, and Compensation on Electron Conduction in Si-Doped κ-Ga_2O_3 Close to the Metal-to-Insulator Transition

Antonella Parisini[1] | Hans Jürgen von Bardeleben[2] | Ildikó Cora[3] | Zsolt Fogarassy[3] | Paola Alippi[4] | Vincenzo Fiorentini[5,6] | Ian Vickridge[2] | Piero Mazzolini[1,7] | Alessio Bosio[1] | Roberto Fornari[1,7]

[1]University of Parma, Department of Mathematical, Physical and Computer Sciences, Parma, Italy | [2]Sorbonne Université, Institut des NanoSciences de Paris 4, Paris, France | [3]HUN-REN Centre for Energy Research, Institute for Technical Physics and Materials Science, Budapest, Hungary | [4]CNR-ISM, Consiglio Nazionale delle Ricerche, Istituto di Struttura della Materia, Roma, Italy | [5]Dipartimento di Fisica, Università di Cagliari, Cittadella Universitaria, Cagliari, Italy | [6]Chair of Nanotechnology, Institute for Materials Science and Max Bergmann Center for Biomaterials, Dresden University of Technology, Dresden, Germany | [7]IMEM-CNR, Institute of Materials for Electronics and Magnetism, Parma, Italy

Correspondence: Antonella Parisini (antonella.parisini@unipr.it)

Received: 23 March 2026 | **Revised:** 24 May 2026 | **Accepted:** 15 July 2026

Keywords: antiphase boundary | metal-to-semiconductor transition | self-compensation effects | Si-doped κ-Ga_2O_3 | ultra-wide-bandgap semiconductor | variable-range hopping

ABSTRACT

Si-doped κ-Ga_2O_3 epilayers grown by metal–organic vapor phase epitaxy on *c*-oriented sapphire were investigated by temperature-dependent resistivity, Hall measurements, electron-paramagnetic resonance (EPR), high-resolution transmission electron microscopy (TEM), and elastic-recoil detection analysis (ERDA). The electrical properties were found consistent with variable-range hopping transport (VRH) through localized states, with the electronic system persisting on the insulating side of a metal-to-insulator transition for any silane flow used. The physical meaning of Hall voltage under hopping transport was critically discussed through the comparison with EPR results. The electronic properties of the samples were described considering the high density of structural defects detected by TEM, hydrogen incorporation found by ERDA, ab-initio calculations, reconciling all results with current literature and with VRH parameters extracted from resistivity data analysis. The conclusion is that most of the Si incorporated in the layers is (self-)compensated, with a compensation ratio higher than 0.9 inhibiting the transition to metal conduction. Structural defects, such as boundaries between rotational domains and off-plane planar antiphase boundaries, are proposed to play a pivotal role in such high compensation via formation of doping-dependent point defects and related deep levels. The role of significant hydrogen incorporation in deep acceptor passivation and compensation reduction is discussed.

1 | Introduction

Gallium Oxide is an ultra-wide bandgap semiconductor with great potential for applications in power electronics, UV radiation solar-blind detection, and photovoltaics [1–3]. Five polymorphs are known [α, β, κ (often named as ε), γ, and δ], most of the research being focused on the thermodynamically stable β-Ga_2O_3, which can be grown as bulk crystals from the melt, in turn allowing for the growth of homo- and hetero-epitaxial layers. The polymorphs differ in crystalline symmetry and different fractions of the Ga atoms with octahedral (Ga-Octa) and tetrahedral (Ga-Tetra) coordination in the unit cell [4]. The monoclinic β-Ga_2O_3 exhibits anisotropy in some physical properties, and its hetero- as well as homoepitaxial growth is challenging [5, 6].

Metastable polymorphs with higher crystallographic symmetry can be obtained through heteroepitaxy on commercially available substrates and are therefore gaining interest [7]. Among them, κ-Ga_2O_3 is particularly attractive because of its peculiar spontaneous polarization along the (001)-direction and its acceptable thermal stability up to about 700°C [8, 9]. κ-Ga_2O_3 is orthorhombic and can be epitaxially deposited on various substrates, but the *c*-plane sapphire is the most employed one [7]. The orthorhombic Ga_2O_3 is characterized by a ratio 1:3 of Ga-Tetra and Ga-Octa sites. The κ-Ga_2O_3 (001) heteroepitaxy on (0001) sapphire results in the formation of 120° in-plane rotated columnar domains, which gives rise to a pseudo-hexagonal symmetry [4]. To avoid the generation of rotation domains, different approaches were attempted, the most successful one being the epitaxial deposition on ε-$GaFeO_3$ substrates [10]. In Ref. [11], the in-plane dimension of the vertically oriented domains has been found to be in the order of a few tens of nanometers in nominally undoped (UD) layers, while the addition of a silane flow Φ_{SiH_4} during the metal–organic vapor phase epitaxial (MOVPE) growth (H_2-carrier gas) allowed for the increase of domain mean size by more than one order of magnitude. In layers with rotational domains, the room temperature (*RT*) in-plane conduction has been demonstrated to be at least one order of magnitude lower than the out-of-plane one. Such anisotropy of the transport properties cannot be explained by the band structure of κ-Ga_2O_3 [12, 13], but is rather attributable to (i) columnar domain boundaries and (ii) other vertically oriented structural defects within the domains [4, 11]. Indeed, anti-phase boundaries (APBs) parallel to (100) planes have been experimentally highlighted and modelled for κ-Ga_2O_3 epilayers on *c*-plane sapphire [4]. High-resolution transmission electron microscopy (HR-TEM) revealed that in the Si-doped samples the average distance among them is about 10 nm [11]. Vyvenko et al. observed similar antiphase boundaries, which they assumed to contain non-saturated bonds, as well as domain boundaries [14], suggesting that both defects may be significant sources of charge carrier trapping and/or compensation. The columnar domains and the defects inside them are then expected to play a role in the prevalence of a hopping mechanism in the in-plane charge transport [11, 15].

This work focuses on the temperature dependence of experimental resistivity, Hall density, Hall mobility, and electron-paramagnetic resonance (EPR) data in Si-doped κ-Ga_2O_3 layers grown by MOVPE on *c*-plane sapphire substrates and with different silane flows Φ_{SiH_4}, extending the *RT* investigation of Ref. [11] on the same samples. The aim of the work is to demonstrate that, notwithstanding the incorporation of a very high density of dopant impurities, the electronic system of these samples persists at the insulating side of the metal-to-insulator transition (MIT) owing to high compensation. The role of structural and stoichiometric defects in promoting compensation and that of hydrogen as an acceptor passivation agent are discussed. The discussion is supported by considering the doping-dependent structural defects detected by HR-TEM investigation. Charge carrier transport is discussed considering the Mott law for variable-range hopping (VRH), analyzing the reliability of the Hall signal in this conduction regime through a crucial comparison with EPR data. The Hall measurements were extended and analyzed at low temperature. Our previously published data were integrated with new data to reach a reliable interpretation of the electronic properties of Si-doped κ-Ga_2O_3 layers grown by MOVPE. Results of elastic recoil detection analysis (ERDA) and ab initio theoretical calculations integrate the framework.

The article is organized as follows:

Section 2 recalls the current knowledge of electronic properties of κ-Ga_2O_3 and literature data needed for overall conclusions of this work in a self-consistent picture. Theoretical and experimental methods are described in Section 3. Experimental data and ab initio density functional theory (DFT) calculations are given in Section 4. The results are discussed in Section 5, organized into subsections.

In Section 5.1, all experimental results, DFT calculations, and previous literature—providing outcomes that are highly interconnected with the new ones—are discussed in the light of high compensation effects and contribute to giving a coherent picture of the electronic properties of the investigated samples.

In Section 5.2, the *RT* data of EPR spin density and Hall carrier concentration were compared as a function of the silane flow, allowing for critical discussion on the reliability of the experimental Hall voltage in evaluating the net doping level in a hopping regime.

Section 5.3 is focused on Hall measurements taken versus temperature below *RT* to compare them with predictions of the percolation theory in the hopping regime approaching MIT [16]. A phenomenological description of the Hall density in the VRH regime to roughly evaluate the localization length of the wavefunction in VRH transport is given in Section 5.4.

In Section 5.5, a phenomenological picture consistent with the presence of structural defects and the experimental mobility trend with Φ_{SiH_4} is proposed.

2 | Current Understanding of Electronic Properties of κ-Ga_2O_3

This section summarizes the main results reported in the literature on the electronic properties of κ-Ga_2O_3 layers, which are preliminary to, and complement, the measurements described in this article. These results sometimes refer to the very same samples discussed here, or to samples deposited via MOVPE under comparable growth conditions. Previous and new results need to be discussed together to provide a consistent picture of the electronic properties of Si-doped κ-Ga_2O_3 layers grown via MOVPE on sapphire.

2.1 | Hopping Transport and Proximity of the MIT

The first evidence of successful n-type doping was highlighted in samples incorporating silicon during the layer deposition [15], whose resistivity data versus temperature resulted non-Arrhenian anywhere in the studied temperature range. These trends and the low Hall mobility values, of a few cm^2/Vs when measurable [13], suggested a transport mechanism through localized states. Indeed, considering the κ-Ga_2O_3 electron effective mass, such values lead to scattering times lower than 10^{-15} s

and mean free paths comparable with the lattice parameters, raising doubts about the applicability of the concept of collision for free electrons. The data were found consistent with VRH transport; however, two VRH regimes have been highlighted, at low and high temperature, called LT-VRH and HT-VRH, respectively, with ~100 K being the border between them. This behavior has been detected in a large quantity of κ-Ga_2O_3 doped samples. Silicon donor was identified as the extrinsic defect that provides the electrons involved in hopping transport and has the properties of a shallow effective-mass impurity [12]. In the same work, the trend of ρ has been supported by EPR data, the resonance being attributed to Si in Ga-Tetra sites owing to the detection of a single EPR line at any temperature. In addition, the evaluation of EPR-detected spin density at *RT* has given similar values to the Hall carrier densities, as for a comparable density of charges involved in the two experiments. The comparison of electrical transport and EPR data suggested to attribute the lower temperature (*LT*) trend to hops between single donor impurities, while the higher temperature (*HT*) trend to hops between donor clusters [12, 13]. This interpretation is in line with the discussion reported in Ref. [17] on donor clusters, which are clouds of a few donors forming in proximity of the MIT transition, in which donors share their electronic states (hybrid wavefunctions with mixed character between extended and localized states). In this frame, electrons are delocalized on the microscopic volume of the cloud but must hop between different donor clusters to travel macroscopic distances. Such spatially limited electron delocalization does not substantially change the mechanism of electrical transport, which anyway takes place by hopping, because extended state conduction needs carrier delocalization on a macroscopic length scale, but it can be detected by EPR measurements because this technique is sensitive to the localization length of the electron wavefunction on short scales [12, 13, 15, 17]. Ref. [17] emphasizes that in proximity to MIT, the formation of donor clusters can justify differences between electrical data and magnetic resonances. Effectively, near *RT*, the EPR linewidth highlights a motional narrowing effect, as for delocalized electrons, with a departure from HT-VRH behavior. This behavior indicated, self-consistently, the proximity of the MIT transition and permitted to roughly estimate the N_c critical density as about 2.5×10^{18} cm^{-3} from the Mott formula $N_c^{1/3} a_0 \approx 0.25$ [12]. These literature data are consistent with the interpretation of transport data in terms of VRH conduction close to MIT.

2.2 | Demonstration of High Si-Incorporation, Located in All Ga Sites

In Ref. [11], the *RT* resistivity, Hall mobility, and carrier density data have been reported for the same samples studied in this work, by varying the silane flow during the growth, showing that VRH transport persists for any Φ_{SiH_4} value. For silane flow higher than 5 sccm, atom probe tomography (APT) demonstrated an incorporated Si density of about 10^{20} cm^{-3}, increasing with the silane flow, without evidence of dopant precipitates in most of the volume. Only close to the layer/substrate interface (confined to a thickness of about 200 nm), TEM highlighted the presence of SiO_x pyramidal precipitates that could influence the effective thickness of the overall in-plane conduction [11]. The *RT* electrical data of this article are reproduced in Figure 1, as reference trends for later discussion on the low-temperature transport data and their variation with silane flow.

Added to this large difference between net and incorporated donor density are the results of photo-electron spectroscopy (PES) and photo-electron holography (PEH) investigation [18], which demonstrated the incorporation of all the detected silicon as substitutional impurity in the four Ga sites, reporting their fractional occupancy and indicating the tetrahedral site as favored. However, the total donor density was not derived. The possibility of a significant fraction of Si impurities in different oxidation states is ruled out; that is, interstitial Si or Si_O (silicon in O sites) defects may exist just in negligible density. Considering the detection of a single EPR donor signal induced Tsai et al. to hypothesize that only Si-donors in tetrahedral Ga-sites are electrically active [18]; they suspected the extended defects inside the domains (i.e., probably electrically charged anti-phase boundaries [4, 14], and the domain boundaries themselves), besides stoichiometric acceptors (V_{Ga} and related complexes), to be majorly responsible of strong compensation (and self-compensation) effects in the Si-doped κ-Ga_2O_3 layers, in analogy to the picture proposed by Fiedler et al. [6] for the β-Ga_2O_3 material system in presence of incoherent twin boundaries.

2.3 | Compensation Effects and Role of Hydrogen

The experimental frame given by the APT, HR-TEM and PES-PEH data is overall consistent with significant compensation in the Si-doped κ-Ga_2O_3 layers. In unintentionally doped samples, a high density of deep acceptors has been observed by cathodoluminescence (CL) [13], photoluminescence (PL) [19] and photoelectrical [13] investigations. The spectra show broad bands extending in the range 1.8–3.2 eV, consistent with transitions from CB or shallow donor levels to families of deep acceptors. Formation energy and energy states of stoichiometric deep acceptors in κ-Ga_2O_3 have been predicted by DFT [19].

It is necessary to note that the effective doping level is also influenced by hydrogen, which can be incorporated from various sources during the MOVPE growth—that is, the carrier gas, the cracking of the metalorganic precursors, water, the hydrogen used for the dilution of the SiH_4, and the cracking of the SiH_4 molecule itself. The hydrogen incorporation during the deposition process could result in an additional extrinsic dopant source, due to (i) a shallow donor behavior (when incorporated in interstitial sites, H_i, or as substitutional to oxygen in its different sites, H_O) and/or (ii) a reduction of the compensation level when H-decorates deep acceptors, for example, forming V_{Ga}–*H* defect complexes in several configurations [19].

In addition, given the low dissociation energy of V_{Ga}–*H* deep acceptors and the possibility to desorb H_i in O-rich annealing atmospheres [19], hydrogen out-diffusion is suggested to play a fundamental role in the observed variation of the electrical properties of the layers upon ex situ heating above *RT*, that is, an irreversible increase of ρ in vacuum/air/O_2 atmosphere described in [13] as well as a change of photodetector characteristics under bandgap and sub-bandgap light excitation [19]. On the other hand, an ex situ annealing treatment in an H_2 atmosphere of nominally undoped layers is found to decrease the ρ of the

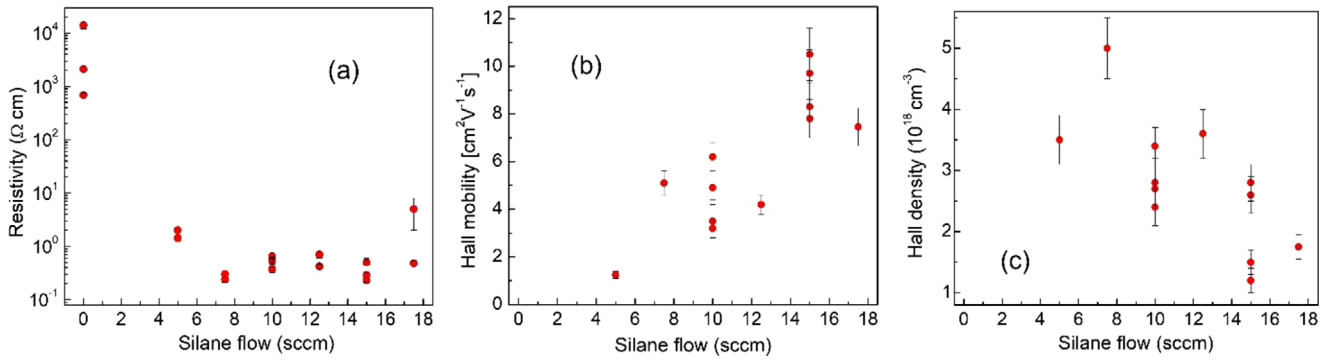

FIGURE 1 | Room temperature (a) electrical resistivity, (b) mobility, and (c) charge carrier density extracted from van der Pauw–Hall electrical measurements of Si-doped κ-Ga_2O_3 layers as a function of the SiH_4 flux employed during deposition (reproduced from ref. [11]).

material [19]. A significant role of hydrogen on the doping level has also been proposed in ref. [20], where a reduction of the net doping profile has been highlighted at the junction interface, on the Ga_2O_3 side, of a diode prepared after heating of the Ga_2O_3 layer.

3 | Methods

3.1 | Experimental

The κ-Ga_2O_3 layers here investigated were grown on *c*-plane sapphire substrates by metal–organic vapor phase epitaxy (MOVPE). Trimethylgallium (TMG) and H_2O were used as metallic precursor and oxidizing gas (precursor pressure ratio: $p_{H2O}/p_{TMG} \approx 350$; partial pressure: 60 mbar; substrate temperature: $T_g = 610°C$); H_2 was employed as gas carrier (2000 sccm, standard cubic centimeters per minute). The deposition time was kept constant for every deposition ($t_{dep} = 100$ min), resulting in about 800–900 nm thick layers. Intentional *n*-type extrinsic doping was carried out by providing during growth a H_2-diluted mixture of 0.05% SiH_4 (Φ_{SiH_4}), maintaining unaltered the other synthesis parameters (Φ_{SiH_4} from 0 to 17.5 sccm). Additional details on these samples can be found in ref. [11], where the results of X-ray diffraction (XRD), Raman spectroscopy, energy dispersive spectroscopy, HR-TEM and APT are also provided.

The κ-Ga_2O_3 layers were electrically characterized in the 10–300 K range by van der Pauw resistivity as well as Hall effect measurements (Keithley Hall-measurement setup, magnetic field of 0.8 T), when the Hall voltage resulted detectable. For this purpose, Ti/Au [15] or SnO_2– Ti/Indium Tin Oxide/Au [21] ohmic contacts were deposited by sputtering technique on the corners of square-shaped samples of about 5 mm sides (ratio between side of the contact and side of the sample ≈ 5), without any sample heating to avoid to alter the sample resistivity [13]. No correction to the electrical data was applied for the finite dimensions of the contacts (further comments in Section 5.2).

EPR measurements have been performed on selected samples in the temperature range 4K–*RT*. An X-band spectrometer (9 GHz) with 100-kHz magnetic field modulation and lock-in detection was employed. The linewidth and amplitude of the resonance were analyzed as a function of temperature, and the absolute values of the spin concentration were obtained by comparison with a spin standard sample. The data were compared with the Hall density and resistivity, according to the suggestion of ref. [12]. Further details on the EPR experiments are reported therein.

TEM experimental data were collected in a Titan Themis G2 200 (Thermo Fisher Scientific) (S)TEM equipped with an X-FEG gun operating at 200 keV and a 4k × 4k CETA16 CMOS camera (Thermo Fisher Scientific). The plan view TEM samples were prepared by conventional Ar-ion beam milling using Technoorg Linda ion millers.

Hydrogen concentration depth profiles were determined by ERDA (SAFIR Ion Beam Analysis platform Institut des NanoSciences of Paris). In ERDA, the energy spectra of protons recoiled from the sample by an incident high-energy alpha particle beam were collected using semiconductor nuclear particle detectors. For the present measurements, a ~100 nA beam of 2 MeV alpha particles was incident on the samples at a glancing angle of 81° from the normal surface. Recoiled protons were detected at the forward angle of 30° with respect to the beam direction. An 8 mm thick aluminum foil in front of the detector stopped the high flux of alpha particles elastically scattered from the heavier nuclei in the target, whilst allowing the more highly penetrating protons to enter the detector. The absolute concentration scale was set using calibrated hydrogen-implanted reference samples.

3.2 | Density Functional Theory for Si-Doped κ-Ga_2O_3

In the κ-Ga_2O_3 phase, Ga atoms occupy four inequivalent lattice positions, one with tetrahedral coordination (Ga-Tetra) and three with approximate octahedral coordination (Ga-Octa) [4]. Specifically, the lattice stacking of (001) planes alternates layers with Ga-octahedral sites and layers with octahedral and tetrahedral sites. The presence of multiple Ga sites with different coordination could influence the incorporation of dopants if, as expected, the latter have different preferential substitutional sites. It was worth noting that in ref. [18] two of the octahedral sites have been named Ga-Octa and the third Ga-Penta. This reflects some literature describing as pentahedral only one (see ref. [22]), but sometimes two (see ref. [23]) of the distorted octahedral sites.

TABLE 1 | *RT* resistivity of the samples investigated in this work. The Table also reports the results of the analysis of the temperature dependence of the resistivity, represented in Mott plots (see Section 5.1.1), according to Equation (1): s_ρ^{HT} (typical accuracy: 1%) and s_ρ^{LT} (typical accuracy: 5%) are the slopes of the two linear trends observed in these plots at high (*HT*) and at low (*LT*) temperature, respectively. The corresponding T_0^{HT} and T_0^{LT} parameters were obtained from these slopes. $|s_n^{HT}|$ denotes the absolute values of the slopes obtained for the *HT* linear trends of the Hall density data in the Mott plot (see Section 5.3), whereas $\ln(n_\infty^{HT})$ represents the intercept of the linear fits with the vertical axis under the assumption of a temperature-independent n_T coefficient (see Equation (2)). In the last column the factor w_{opt}^{HT}/KT is calculated from $|s_n^{HT}|$: it is related to the impurity bandwidth normalized to *KT*. The scattering of the experimental data resulted in an uncertainty on the slopes lower than 5%.

Sample n.	Φ_{SiH_4} (sccm)	ρ at *RT* (Ωcm)	s_ρ^{HT} ($K^{1/4}$)	T_0^{HT} (K)	s_ρ^{LT} ($K^{1/4}$)	T_0^{LT} (K)	$\lvert s_n^{HT}\rvert(s_\rho^{HT}/\lvert s_n^{HT}\rvert)$ ($K^{1/4}$)	$\ln(n_\infty^{HT})$	$\frac{w_{opt}^{HT}}{K_BT}$
531	0	750	99.3	9.72×10^7	—	—	—	—	$103.3/T^{1/4}$
527	5	1.46	20.8	1.87×10^5	8.7	5728	—	—	$5.20/T^{1/4}$
521	7.5	0.18	5	6.29×10^2	2.3	27.9	—	—	$1.25/T^{1/4}$
505	10	0.49	7.7	3.57×10^3	2.3	26.7	2.51 (3.1)	43.03	$1.93/T^{1/4}$
507	12.5	0.42	11.5	1.75×10^4	4.1	287.0	2.91 (4)	43.42	$2.88/T^{1/4}$
506	15	0.28	9.3	7.35×10^3	2.9	72.6	3.4 (2.7)	43.27	$2.32/T^{1/4}$
508	15	0.21	7.9	3.8×10^3	2.1	20.1	2.44 (3.2)	43.06	$1.98/T^{1/4}$
510	17.5	0.49	10.4	1.16×10^4	4.4	362.4	3.33 (3.1)	42.79	$2.60/T^{1/4}$

We performed calculations within DFT as implemented in the Vienna Ab-Initio Simulation Package (VASP) code [24], with projector augmented-wave potentials [25] and the Heyd–Scuseria–Ernzerhof (HSE) hybrid functional, using $\alpha = 0.32$ and $\mu = 0.2$ [26]. We used an energy cut-off of 400 eV, a $(2\times2\times2)$ *k*-point mesh and the 80-atoms supercell built up as a $2\times1\times1$ repetition of the 40-atoms unit cell of κ-Ga_2O_3, which provided a reasonable distance between periodic replicas of the defects. The calculated equilibrium lattice constants ($a = 5.048$ Å, $b = 8.67$ Å, $c = 9.26$ Å) were in good agreement with experiment. The calculated gap of 4.91 eV agrees with experiment; we pointed out that in general the gap was sensitive to the specific treatment of electron–electron interaction and to the attendant changes in predicted volume, as discussed, for example, for β-Ga_2O_3 [27].

4 | Results

4.1 | Transport and EPR Data

Resistivity and Hall effect measurements in a wide low-temperature range were performed on several Si-doped samples grown under different silane fluxes. Typical uncertainty in the resistivity and in Hall data was evaluated, respectively, to be 5%–10% and 10%, based on the reproducibility of the measurements in different pieces of samples for varied injected currents, and on the ratio between dimensions of the contacts with respect to the sample sides, as already discussed in ref. [11]. Error bars at *RT* are shown in Figure 1 for the same samples. Since the temperature dependence of the data is weak, the same uncertainties apply to the data at each temperature. The list of the samples investigated in this work is reported in Table 1.

Figure 2 shows the temperature-dependent resistivity data of these samples represented in a Mott plot, that is, the plot of a physical quantity on a natural logarithmic scale versus $T^{-0.25}$, in which they show linear trends.

Figure 3a,b report the EPR resonance in the nominally undoped sample and a doped one obtained for two orientations of the magnetic field, parallel and perpendicular to the *c*-axis of the orthorhombic cell. The typical EPR spectra at different temperatures are given in Figure 3c,d for selected doped samples. Figure 3e,f display two examples of the temperature dependence of the EPR linewidth, reported in a Mott plot. Comparable data were obtained for the other doped samples.

As concerns the Hall voltage, it is often non measurable in the hopping regime [28, 29]. It was never detectable in nominally UD Ga_2O_3 layers. However, in the doped samples here discussed, the Hall voltage was measured at *RT* and in a wide range of temperatures below *RT*, resulting in the Hall density and mobility data reported by Figures 4 and 5 for some silane flow values. The physical meaning of the Hall voltage in VRH transport was discussed by Castner [16], as recalled in Section S1. In Section 5.2, this critical point is experimentally discussed through comparison with spin density data from EPR investigation. For this analysis, the dependence on Φ_{SiH_4} of the *RT* EPR linewidth and the spin density derived by the EPR signal intensity are respectively reported in Figure 6a with the trends of *RT* conductivity and in Figure 6b with the *RT* Hall density data.

It can be noted that, since the density of incorporated Si varies sub-linearly but monotonically with Φ_{SiH_4}, similar trends for data of Figure 1 and Figure 6 would be obtained as a function of the Si-content in the samples.

4.2 | TEM Investigation

The Introduction reported that, in (001) oriented κ-Ga_2O_3 layers deposited on sapphire, planar defects form inside each rotational domain parallel to (100) planes (yellow boundaries and red lines, respectively, in Figure 7a), with a relative distance of about 10 nm on average. These extended defects are delimited by anti-phase boundaries [4, 14], and Figure 7b shows that the stacking

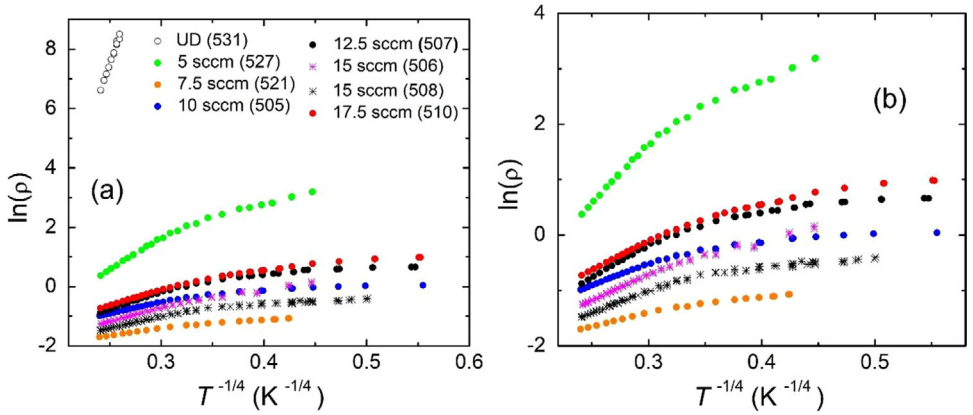

FIGURE 2 | (a) Temperature dependence of the natural logarithm of the resistivity (in Ω cm) for the samples here investigated (see Table 1) deposited without and with Φ_{SiH_4} versus $T^{-1/4}$ plot (Mott plot). (b) Zoom of (a) reporting only data relative to intentionally Si-doped samples.

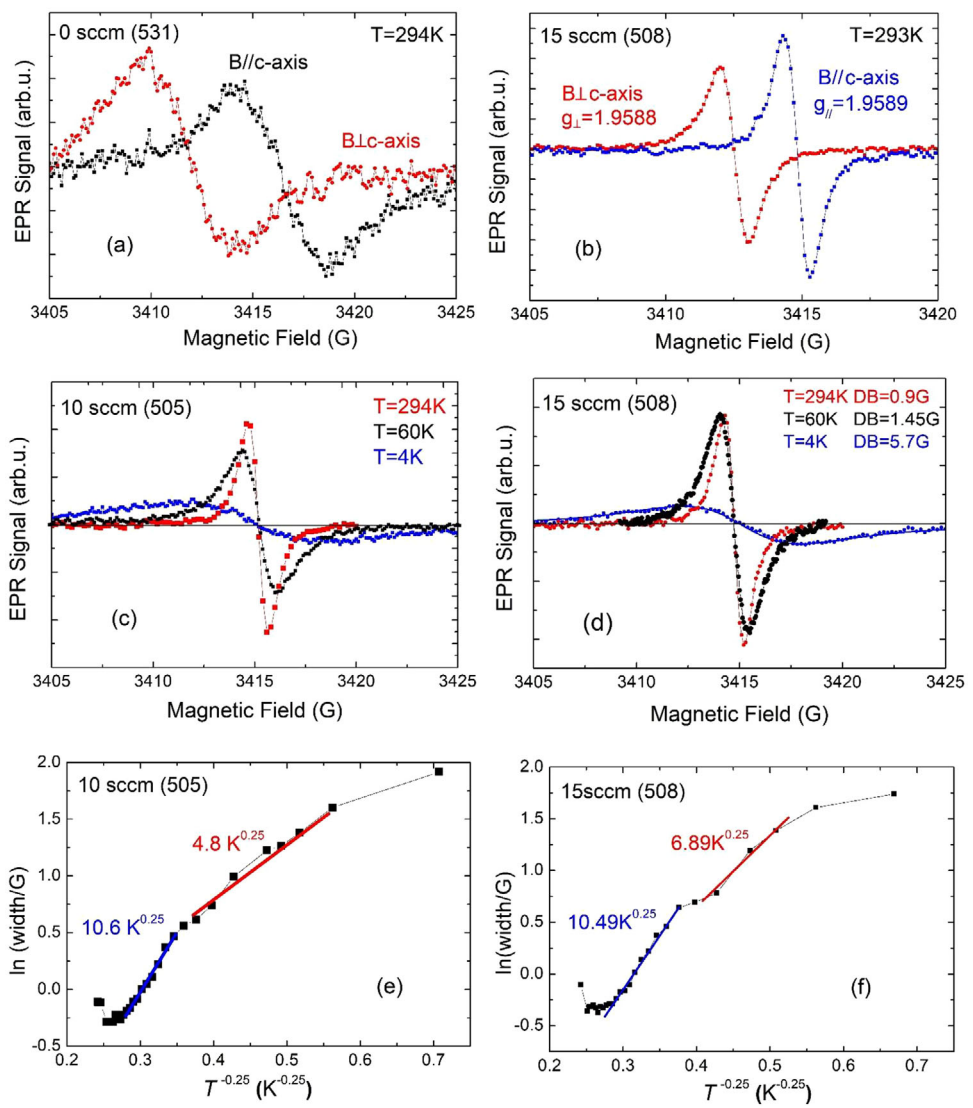

FIGURE 3 | EPR spectra of the donor for $B \perp c$-axis and $B//c$-axis in (a) for the 531 nominally undoped sample, $T = 294$ K, in (b) for the Si-doped sample 508 (15 sccm) at $T = 293$ K with indications of the respective g-factors. EPR spectra of the donor at different temperatures in (c) for sample 505 (10 sccm) and in (d) for sample 508 (15 sccm); the linewidth ΔB are reported. In (e,f): Mott plots of the EPR linewidth in G, ln (width/G) versus $T^{-0.25}$ ($K^{-0.25}$): in (e) for sample 505 (10 sccm) and in (f) for sample 508 (15 sccm). The slopes of the two linear trends drawn at *HT* and *LT* are reported.

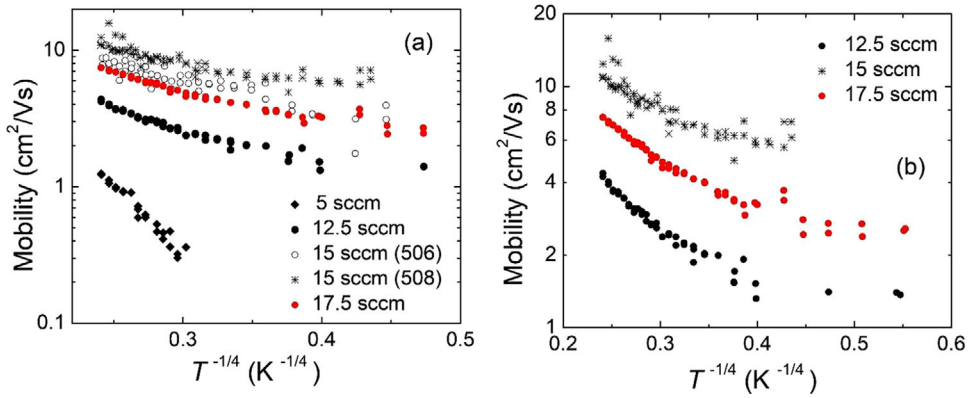

FIGURE 4 | (a) Temperature dependence of the mobility, in logarithm scale versus $T^{-1/4}$, for some samples here investigated (see Table 1). The line is a guide for eyes. (b) Selected data are plotted on an expanded scale to better evidence the two linear traits, using the same symbol for each sample as in (a).

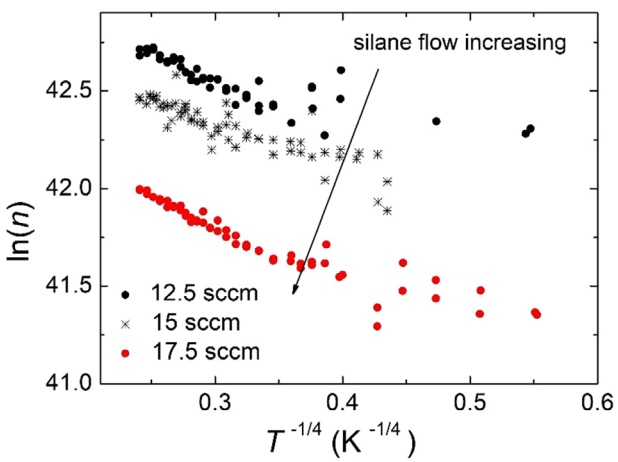

FIGURE 5 | Temperature dependence of the natural logarithm of the Hall density (in cm^{-3}) versus $T^{-1/4}$, (Mott plot) for some of the doped samples here investigated; the same symbol for each sample is used as in Figure 4a. The data of sample 506 (15 sccm) are very similar to those of sample 508 (15 sccm): they are not reported for clarity.

sequence of the Ga planes between APB boundaries, without distinguishing here between tetrahedral and octahedral sites, changes from ABABA to ABAAABA, that is, the position and ordering of the Ga sites is different; meanwhile, the hexagonal sublattice of oxygens does not change. In principle, no bonds were cut, although defects cannot be excluded. The thickness of these APBs is within ~1.5–2 nm (3–4 × |*a*| = 3–4 × 5.2 Å, |*a*| is the length of *a*) and they run through the whole grain/domain parallel to (100) plane (i.e., parallel to *b*- and *c*-directions) but never cut the grain/domain boundaries. Their propagation along the *c*-direction is sometimes connected to SiO_x precipitates that are though located just in a region close to the substrate interface [11].

Interestingly, from higher-resolution plan-view samples, sometimes the anti-phase boundary shifts in *a*-direction of $n \times |a|/2$ (ca. 2.5 Å), afterward, it keeps the direction (|| to (100)). These defects in APB (let's call "APB shift-defect") are evidenced in Figure 7a with little circles and sketched in Figure 7c; note that they propagate in the *c*-direction. Even in the APB shift-defects the O sublattice is continuous without any fault; only the order of occupied positions has been changed. However, such a shift opened a larger space (i.e., an unoccupied Ga position), although the Ga/O remained 2/3. It cannot be excluded that a dangling bond could be located therein.

Similar defects have been highlighted in ref. [14]. However, in this study we point out that the fraction of APBs with shift-defects increases with the silane flow: in the undoped sample (0 sccm) about 10% of APBs contained shift-defects; while in the 5,15, and 17.5 sccm samples the fraction increased to about 25%, 60%–80%, and 80%–100%, respectively. Moreover, in some APBs there was more than one shift-defect. Figure 7d shows the enhancement in surface density of APB shift-defects (in APB shift-defects/nm^2) with respect to Φ_{SiH_4} increasing. Squared surfaces with sides of a few hundred nm (about 200 and 300 nm for low and high Φ_{SiH_4} values, respectively) were considered representative for the estimation, averaging over several domains in all cases. Since the number per unit area of APB defects was found to slightly reduce with Φ_{SiH_4}, probably owing to the domain enlargements, the average number of APB shift-defects per APB defect resulted in increasing super-linearly with Φ_{SiH_4}. Note that no variations in the local Si density was highlighted in the presence of defect sites by atom probe tomography [11].

4.3 | ERDA Investigation

Hydrogen can be incorporated into the epitaxial layers from the carrier gas and from the nutrient phases during MOVPE growth of the films and can have effects on their *net* doping level. A preliminary ERDA investigation was performed to demonstrate the hydrogen incorporation in the layers. Figure 8 shows the ERDA profile on two representative samples. Note that the high hydrogen peak observed near the surface in each sample includes a small environmental contamination. There is accumulation of hydrogen near the layer surface in the as-grown samples, with each profile flattening out into a plateau in the bulk of the samples at a level higher than the instrumental background, exceeding the detection limit of the technique, up to the 200 nm explorable depth. In the bulk of other samples, however, the hydrogen

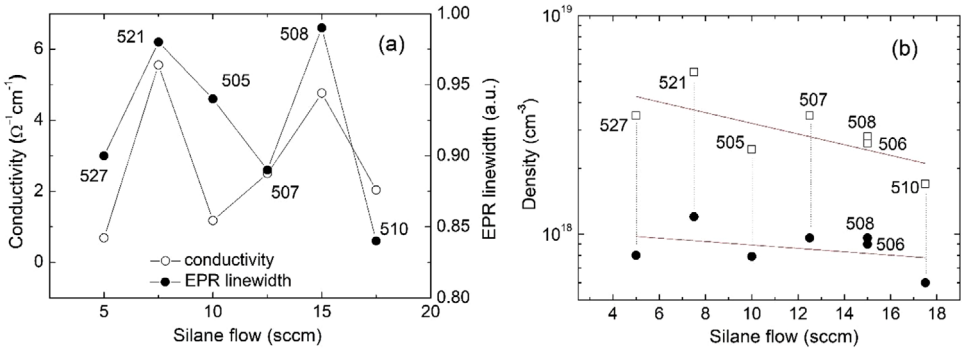

FIGURE 6 | Room temperature (a) conductivity (in 1/Ω cm) and EPR linewidth (in a.u.) versus silane flow (in sccm), (b) Hall density (open square) and spin concentration (full circles) obtained from the EPR spectra; absolute values were obtained by comparison with a spin standard sample. Linear trends are guides for the eyes.

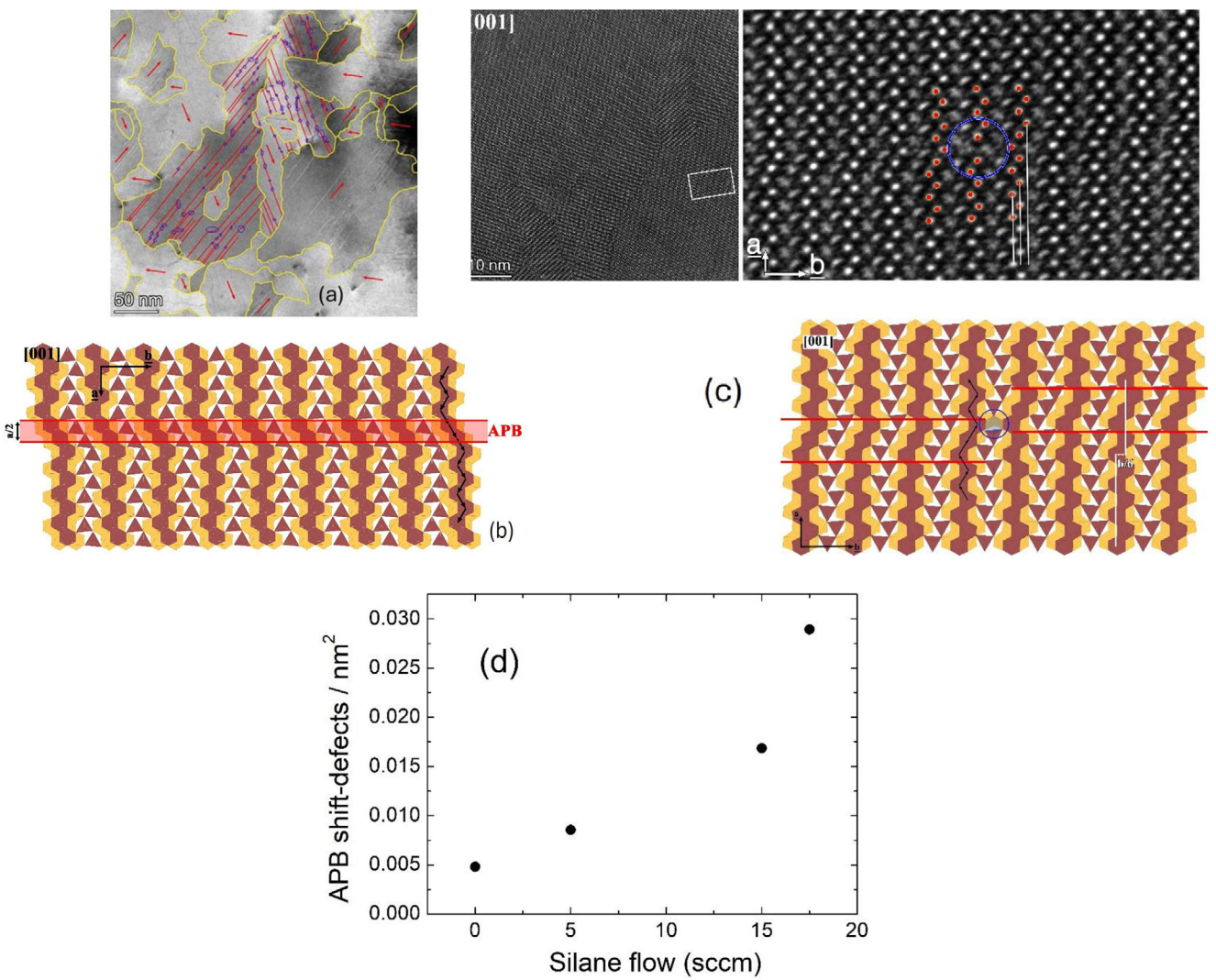

FIGURE 7 | (a) Plan view TEM image in [001] projection (image plane is parallel to substrate surface). Domain boundaries are marked by yellow lines, and some anti-phase boundaries are signed by red lines. Blue circles indicate APB shift defects (regions where the APB shifts, see text). The APBs are parallel to (100) planes, in the above image parallel to the *b*-direction of the orthorhombic lattice (red arrows on TEM image). In the Supporting Information, the same figure is reported without blue circles and red lines for a better view of the TEM image (Figure S1). (b) Polyhedral representation of an implemented APB (see text). (c) Enlarged picture of an APB shift-defect on [001] projected experimental High-Resolution TEM images with the corresponding structural model (rectangle on the HRTEM image signs the place of the enlarged inset on the right). Blue circles indicate APB shift-defects (regions where the APB shifts, see text). (d) Silane-flow dependence of the number of APB shift-defects per nm^2, having considered squared surfaces of a few hundred nm sides for the estimations.

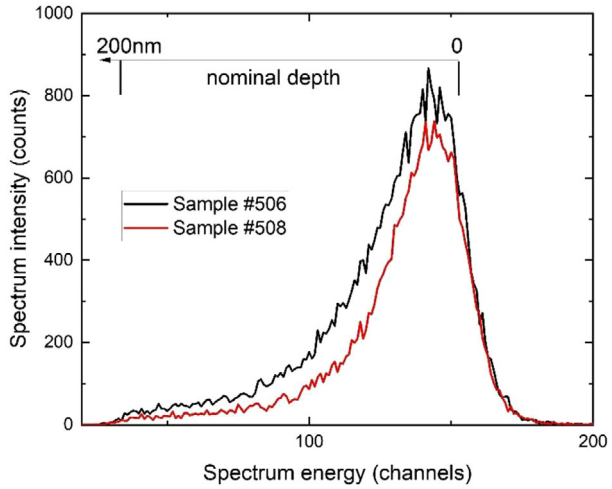

FIGURE 8 | ERDA profiles measured in two representative Si-doped samples.

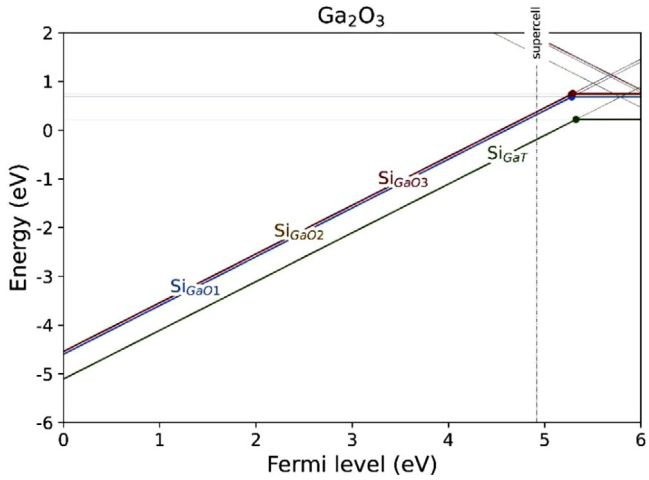

FIGURE 9 | DFT-HSE formation energies for charged Si_{Ga} configurations as a function of the Fermi energy.

level resulted below the instrumental detection limit. Overall, a hydrogen density in the range of $10^{19}\,cm^{-3}$ can be roughly estimated in the sample series. However, not all incorporated hydrogen is necessarily electrically active. These preliminary measurements did not show a trend of hydrogen incorporation with the silane flow.

4.4 | DFT Analysis

Our HSE total energy calculations for substitutional Si_{Ga} show that Si sits preferentially on tetrahedral sites (Si-Tetra). The three Si_{Ga} octahedral sites (Si-Octa) are disfavored by about $\Delta E = 0.45$ eV compared to Si-Tetra. Using equilibrium thermodynamics at a typical growth temperature ($T_g = 610°C$), we obtain a concentration ratio of Si-Tetra to Si-Octa of about 90: 10. We accounted for the threefold site degeneracy and the configurational entropy ($dS = \log 3$) of Si-Octa, which increases their concentration roughly 10-fold. This prevalence of Si-Tetra sites seems rather natural given the preference of Si for tetrahedral O coordination, for example, in SiO_2; also, it is consistent, as discussed below, with EPR measurements. The calculated ratio is considerably larger than the 55:45 (i.e., Si-Tetra over the sum of Si-Octa and Si-Penta) reported in Ref. [18].

A second important result is that Si_{Ga} is a shallow or resonant donor on all four substitutional sites. The quantitative indicators of this behavior are the thermodynamic charge transition levels $\varepsilon_{q/q'}$ computed from defect formation energies of charged Si_{Ga}. These calculations are done at variable electron numbers and need corrections for artificial interactions between charged defects in periodically repeated supercells, which we apply using the method of Freysoldt et al. [30].

Figure 9 reports on the formation energies of the different charge states of the various sites as a function of the Fermi level. From Figure 9 it is apparent that, first, the favored site is always Si-Tetra (we chose intermediate growth conditions producing a concentration of around $10^{19}\,cm^{-3}$ [31], approaching the experimental net donor density, although without taking into account compensation and disorder). Second, the relevant transition level is $\varepsilon_{+/0}$, characteristic of an unoccupied/occupied donor state (the levels $\varepsilon_{+/-}$ typical of negative-U behavior are about 0.5 eV higher in energy). The $\varepsilon_{+/0}$ level is at +0.48 eV with respect to the CB bottom for Si-Tetra, and similarly for Si-Octa. Since for all configurations the calculated $\varepsilon_{+/0}$transition level is within the conduction band, positively ionized Si_{Ga} defects are stable for the whole range of electron chemical potential, and electrons are released into the conduction band.

Although similar to that obtained for Si in β-Ga_2O_3 in Refs. [32] and [33], this conduction-resonant impurity state is relatively uncommon. We therefore checked carefully whether it could be affected by computational ingredients. Changes in the α parameter of HSE between 0.25 and 0.35 do not appreciably affect the thermal levels (i.e., the gap and the thermal levels shift together), nor the energy differences between sites. The quantities reported are similarly insensitive to changes in the PAW datasets for the atoms involved. They are also insensitive to further refinements of the k-point grids (we tested convergence in the computationally affordable GGA/GGA+U scheme). We conclude that the results, and the thermal levels in particular, are indeed computationally robust.

5 | Discussion

5.1 | Resistivity and EPR Data Versus Temperature

When represented in an Arrhenius plot, the resistivity curves of the samples exhibit a continuously varying slope, consistent with temperature-dependent activation energy, which is frequently ascribed to a VRH mechanism [34]. This attribution is consistent with the low mobility values measured, typical of electrical transport between localized states, as mentioned in Section 2.1. A useful procedure for identifying the prevailing hopping mechanism (Section S1 gives a review on hopping transport) would be to analyze the temperature dependence of the derivative $d\ln(\sigma)/d\ln(T)$, as applied in Refs. [35, 36], which however in this contest did not lead to convincing results due to the limited range

of resistivity variation. On the other hand, in this work we do not want to speculate on the details of the hopping mechanism, but rather to demonstrate its persistency for any silane flow and correlate this result with the proximity to MIT and the presence of disorder/high compensation that inhibits the occurrence of the transition. A VRH transport mechanism is effectively expected in proximity to MIT [37]. As linear trends are observed when the data are plotted on a natural logarithmic scale versus $T^{-0.25}$ [15], as Figure 2 shows, the Mott law (Equation (1S) with $n = 4$, i.e., 3D Mott-VRH) was adopted, that is,

$$\sigma\ (T) = \sigma_0 \exp\left[-(T_0/T)^{1/4}\right] \tag{1}$$

here T_0 is a reference temperature defined as $T_0 = C(\xi^3 g_F K_B)^{-1}$, depending on g_F, that is, the energy state distribution next to E_F assumed constant for negligible electron–electron interaction [28, 29], and on ξ, that is, the localization length of the states close to the E_F. σ_0 and ξ are assumed to be energy independent [28]; K_B is the Boltzmann constant. The proportionality constant C is a dimensionless parameter that accounts for details of the hopping site network presumed in the model of transport. It was assumed equal to $8^3/9\pi \approx 18.1$, as for randomly distributed hopping sites (see Ref. [36] for a deeper discussion). Following [38], the energy states involved in the transport lie in a band around E_F having a temperature dependent width comparable to the quantity $w_{opt} = (K_B T/4)\,(T_0/T)^{1/4}$, often called "optimum energy", so that the product $N_S = g_F\, w_{opt} = (C/4\xi^3)\,(T/T_0)^{3/4}$ represents the density of hopping sites in such a band at a given temperature, finally, the average hopping length, often called "optimum length", is $R_{opt} = (3/8)\xi\,(T_0/T)^{1/4}$. If the density of states g_F is assumed constant within an energy range of $\pm\, W$ around E_F, where $2W$ represents the impurity bandwidth, it can be defined as: $g_F = g_{avg} = N_D/2W$ for $|\varepsilon - E_F| \leq W$ and $g_F = 0$ outside this range [28]. Such a rough definition of g_{avg} highlights the competing effects on g_F of both the density of electrically active centers (the doping level) and disorder, which spreads the energy states, favoring carrier localization and increasing of W. The list of formulas and acronyms used in this work for VRH transport is summarized in Section S2.

In accordance with previous literature [12, 13, 15], most of the curves in Figure 2 show the two *HT*-VRH and *LT*-VRH linear trends, at higher and lower temperatures, limiting the possibility to study the transport mechanism more precisely. EPR investigation performed on the same samples confirmed this behavior, as Figure 3e,f shows for two selected layers. The temperature dependence of the EPR linewidth is reported as a function of the temperature (in the range *RT*–4 K) in Mott plots, which show double linear trends with slopes comparable to those already observed in EPR investigations [12] and similar to those exhibited by resistivity data (see Section 2.1, for the interpretation given of the double linear trends). A weak anisotropy of the EPR spectrum (see Figure 3a,b) is also observed, corroborating the results of Ref. [12].

Only the electrical properties of the undoped sample (sample 531 in Table 1) were measurable in a very limited temperature range. It is worth noting that its *RT* resistivity (10^3 Ω cm range) is appreciably lower than the usual resistivity of samples grown under the very same growth parameters ($\rho \approx 10^5$ Ω cm [11]). Such lower resistivity was probably related to the unintentional incorporation of residual impurities of the extrinsic dopant (silicon) supplied in immediately preceding growth runs. This is in line with the results of the EPR investigation, which detected in the 531 sample a donor resonance (see Figure 3a) like those revealed in Si-doped samples [12] and never observed in nominally undoped samples. Notwithstanding this, data of the 531 sample have been added in this plot as a nominally UD sample to give an example of a resistivity trend versus low temperature that occurs when size and distribution of domains are typical of layers deposited without silane flow [11]. More resistive samples were never measurable below *RT*. Other comments on Figure 2a are reported in Section S3.

VRH parameters consistent with Equation (1) were extracted from the electrical data versus Φ_{SiH_4} to deduce the variation of the main features of the impurity band (IB) with the growth conditions, testing the coherence of the interpretative frame. *LT* and *HT* trends of the resistivity Mott plots were linearly fitted for the samples investigated, and the corresponding slopes, s_ρ^{LT} and s_ρ^{HT}, are reported in Table 1. An uncertainty of about 5% can be assumed for *LT* slopes and of 1% for *HT*, although the absolute values of the data have an uncertainty related to the dimensions of the contacts in the van der Pauw method (see Ref. [11] and discussion in Section 5.2). Each slope can be assumed equal to the product $C(\xi^3 g_F K_B)^{-1/4}$ in the corresponding *LT* or *HT* range, respectively. Fluctuations that appear in these data as Φ_{SiH_4} varies, may be attributed to tolerances on the growth process parameters, as will also be commented in Section 5.1.2 for the data of Figure 6.

In the same Table, the factor w_{opt}^{HT}/KT is reported, related to the optimum energy for *HT*-VRH. The IB-width was estimated from the equation: $W \approx 2w_{opt}\,(T) = 0.5K_B(T^3 T_0)^{1/4}$ for $T = 300$ K, since it was not possible to heat the samples up to the temperature necessary to determine the critical T_ν beyond which VRH is no longer observed [39–43]. As recalled in Section S1, the experimental measure of T_ν can provide a convincing estimation of the IB-width; however, in this work any investigation above *RT* was avoided, because heating would have induced an irreversible increase of the sample resistivity, probably caused by hydrogen out-diffusion [20]. Nevertheless, VRH certainly persists above *RT* [13]. The estimation $W \gtrsim 2w_{opt}(300\,K) \approx 20$ meV is obtained, which is comparable/lower than the expected fundamental energy state for a hydrogenic donor in κ-Ga_2O_3, calculated in effective-mass approximation, that is, $E_B = 0.03$ eV [12, 13]. Therefore, a broad IB is expected to overlap with the CB states, merging with them and forming a band tail of localized states, near which E_F must lie, consistently with the activated transport [17]. The compensation ratio establishes the position of the E_F within the localized states.

5.2 | Resistivity and EPR Data Versus Silane Flow

Concerning silane-flow dependence of the resistivity, the curves of Figure 2 are consistent with those shown by Figure 1a in Section 2.3, with $\rho(T)$ data decreasing of several orders of magnitude in absolute value as Φ_{SiH_4} increases from 0 to 5 sccm. We call this behavior of the resistivity as regime (a), not explored in detail in this work; it is followed by an almost flattened trend of ρ for $\Phi_{SiH_4} \geq 5$ [regime (b)]. The $\rho(T)$ curves in the latter

regime are nearly superimposed, with fluctuations in the ρ data as Φ_{SiH_4} varies that are likely related to the tolerance on the growth-process parameters (as mentioned above). Indeed, they are outside the experimental uncertainty in the measurements and independent of the experimental technique, as shown in Figure 6a. In this figure, the fluctuations in ρ are correlated with similar fluctuations of the EPR linewidth values, plotted on a proper scale, at the same temperature. The reliability of the comparison is based on the agreement between these quantities shown in Refs. [12] and [13]. A hint of a *RT* resistivity increasing can be cautiously noticed at the highest silane flow value, $\Phi_{SiH_4} = 17.5$ sccm.

The evolution from regime (a) to regime (b) is also related to the significant reduction of the slopes s_ρ^{HT} estimated for sample 531 (0 sccm) and sample 527 (5 sccm), shown in Table 1. Combined with the simultaneous decrease of the absolute value of the resistivity shown by Figure 1a, these features indicate that the regime (a) is characterized by a relevant increase of the net doping level and of the carrier density of several orders of magnitude with Φ_{SiH_4}. Indeed, in UD layers the density is below the detectability limit, whereas Hall density values of a few 10^{18} cm^{-3} are obtained at the onset of regime (b). Although samples of intermediate sccm values in the range 0–5 sccm are lacking in this series, the above conclusion can be qualitatively supported by similar transport data obtained in Sn-doped κ-Ga_2O_3 samples, where the *n*-type doping has been obtained ex situ by diffusion [15, 44]. Hall densities in the order of 10^{17} cm^{-3} were detected for some samples of Ref. [15], whose absolute resistivity values and corresponding s_ρ^{LT}, s_ρ^{HT} slopes resulted self-consistently higher than those of the doped samples here discussed. In the light of the definition $g_{avg} = N_D/2W$, the variations of s_ρ^{LT} and s_ρ^{HT} slopes in regime (a) agree with the conclusion that the density of the states of the IB, g_F, is mainly controlled by net doping level increase, with minor effects of disorder increasing on *W*. However, these decreases in slope are fully attributable to variations in g_F only under the evidence of a weak dependence of the localization length ξ on Φ_{SiH_4}, because in the Mott theory s_ρ^{LT} and s_ρ^{HT} are inversely proportional to the factor $(\xi^3 g_F)^{1/4}$ (as ${T_0}^{1/4}$). In Section 5.4 specific considerations will be made on ξ for the samples of this work, supporting the above assertion.

Differently, in regime (b) the values s_ρ^{HT} and s_ρ^{LT} reported by Table 1 for $\Phi_{SiH_4} \geq 5$ sccm show a weak tendency to increase, also summarized in Figure 2S, interpretable as g_F decreasing/saturation. We observe that, in this regime, the Hall density remains in the 10^{18} cm^{-3} range for any Φ_{SiH_4}, despite the increasing Si-incorporation indicated by APT investigation [11] and the detection of Si-impurities only in Ga sites [18], resulting in donor defects (see Sections 2.2 and 2.3 for further comments). Considering that the critical density for the MIT is of the order of 10^{18} cm^{-3} [13], the experimental frame is compatible with the approaching of the MIT for any Φ_{SiH_4} in regime (b), never crossing the transition, owing to an increasing compensation level. This should imply that ξ remains almost constant (as indeed it turns out in Section 5.4), since the scaling laws predict a ξ enhancement as MIT is approached, while a nearly constant value of ξ should indicate a quite unvaried proximity of the electronic system to the MIT for any Φ_{SiH_4}. In conclusion, the plateauing of the resistivity is consistent with the inhibition of the transition for any Φ_{SiH_4}, as for a MIT mainly controlled by disorder (Anderson localization) and a compensation ratio approaching unity [45, 46] (see also Section S1. This is corroborated by EPR results. Since the EPR signal is sensitive to the localization length of the electron wavefunction on short scales, it is less affected by disorder; then, at high temperature, it shows delocalization of the donor electrons. This is evidenced in Figure 3c,d where, at *RT*, the EPR linewidth is significantly reduced by the motional narrowing effect (see Section 2.1). Due to the same effect, in Figure 3e,f the linewidth becomes nearly constant near *RT*. The motional narrowing effect can be considered as a fingerprint of MIT.

A trade-off between increasing disorder and doping level for increasing Φ_{SiH_4} may justify the trend of all the data in regime-(b), the disorder assuming a dominant role over doping in $g_{avg} = N_D/2W$ for $\Phi_{SiH_4} \geq 5$, through high compensation and widening of *W*.

5.3 | Remarks on Compensation

The purpose of this section is to reconcile the observation that EPR investigations detected Si only in Ga-Tetra sites [12] with the requirement that compensation leaves the impurity states at higher energies unoccupied, implying that the occupied Si-Tetra states lie at lower energies than the other Si_{Ga} donor states.

High levels of doping and disorder may induce carrier localization on donors with broadening of the energy states into an IB and hopping transport. In the presence of different donor sites (i.e., the different Si_{Ga} donors), an overlap of their impurity states can be expected, depending on their relative energy positions. It is noteworthy that, in the limit of diluted impurities and absence of disorder, DFT predicted hydrogenic character of all the Si_{Ga} donors (Section 4.4) as well as similar features for the lowest transition levels of Si in the four Ga-sites. Since TEM investigation (and APT analysis in Ref. [11]) showed no accumulation of Si at extended defects (e.g., APBs and domain boundaries) but rather a uniform distribution of the dopant within the conducting layer, disorder should produce similar effects—on average—on the impurity levels of all Si_{Ga} donors, broadening them into bands centered at energies below the CB minimum, with bandwidths depending on the concentration of each Si_{Ga} donor species. All the bands are convoluted into a global IB. Qualitative information on such an IB was obtained from the analysis of $\rho(T)$ in the frame of the Mott theory.

The picture emerging from the discussion of Sections 5.1.1 and 5.1.2 and the DFT calculation is summarized in Figure 10, which gives a qualitative sketch of the allowed density of states (DOS) at the bottom of the conduction band (CB), drawn following Refs. [39–43]. Two Gaussian-shaped IB are assumed for the Si_{Ga} donor states, having integrated areas proportional to the DFT-calculated abundance of each Si_{Ga} donor, that is, 90% for Si-Tetra and 10% for the Si-Octa. For the donor electrons, the energy states are assumed below the band edge, owing to disorder-induced localization; the peak of their convolution (IB-total) is separated by a few tens of meV from the CB extended states, according to the IB-width *W* roughly estimated above. However, owing to its lowest formation energy, the density of Si-Tetra states is expected to be the highest and the corresponding IB broader than the others, defining the low-energy tail of IB-total. Because of the

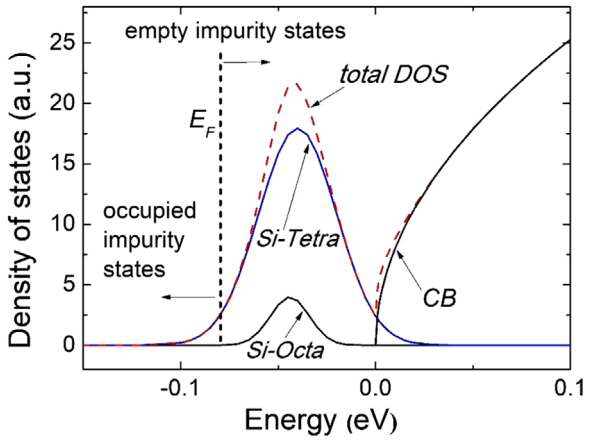

FIGURE 10 | Sketch of the total DOS due to the superposition of the four IBs due to the Si_{Ga} states (assumed with a Gaussian profile) and the CB states (assumed to have an ideal $\sqrt{E}$ profile): the IB associated with Si-Tetra has a higher density of states and is more widespread; E_F lies in the tail of this band (which is also the tail of the total IB); the states below the Fermi level are occupied, and the other are emptied by compensation. The energy positions of all IBs have been fixed at similar energies at about −0.04 eV, assuming four shallow donors as suggested by DFT calculations, with an IB-width consistent with the rough estimate above. However, in the limit of insulated donors and absence of disorder, the energy states are expected to be resonant with the CB states (Section 4.4).

high compensation, the Fermi level is expected to intersect this tail, as illustrated in Figure 10, suggesting that even the donors associated with the Si-Tetra IB are largely compensated. In this schematic picture, CB is represented by a qualitative $D(E) \propto \sqrt{E}$ profile, while the actual spectral weight and continuity between the total IB and the CB are not treated quantitatively. In a more rigorous representation, the CB should deviate from the $\sqrt{E}$ trend, incorporating the impurity states into a CB band tail. Nevertheless, these states are expected to be nearly depleted by the strong compensation, causing the Fermi level to intersect the deeper localized states associated with Si-Tetra donor states.

If the presence of both Si-Tetra and Si-Octa proposed in Ref. [18] is considered, a similar picture with the Fermi level falling in the tail of the Si-Tetra DOS could be qualitatively proposed. In this picture, other background donors such as oxygen vacancies (V_O) are neglected because their density is much lower than that of Si-donors.

Given the Si concentration in the range of 10^{20} cm^{-3} and increasing with Φ_{SiH_4} [11] but only resulting in a *net* donor concentration of a few 10^{18} cm^{-3}, a high compensation ratio $K = N_A/N_D \approx 0.99$ is deduced. This value of K may be overestimated. In fact, although in Ref. [18] interstitial-Si or different Si-oxidation states are ruled out, as recalled in Section 2.2, a small fraction of other defects involving Si could exist. However, K would still be very close to unity. Such a high compensation is supposed to inhibit the transition to metal conduction, maintaining the Fermi level into the IB, and the system at the insulating side of a MIT, according to experimental [45] and theoretical [46] results of the literature (see Section S1). In this regime, VRH transport is expected [37], characterized by finite ξ-values.

Thinking about the origin of this high compensation, we observe that a significant presence of deep acceptors is expected in the Si-doped layers of this work, consistently with the results of CL [13] and PL [19] and with a significant sub-bandgap responsivity signal [13] obtained in UD layers grown under similar conditions. The formation of stoichiometric point defects of acceptor type, such as V_{Ga} and split Ga-vacancies, is also predicted by the DFT results reported in Ref. [19] for nominally undoped κ-Ga_2O_3 and may explain a significant compensation. Their overall density may be expected to be comparable with the one found in β-Ga_2O_3, that is, around 10^{18} cm^{-3} [47]. But such concentration is far too low to account for the estimated compensation in the present samples, that contain ≈10^{20} cm^{-3} Si atoms compensated for over 90%.

It is necessary to postulate the presence of further defects, for example, electrically-active structural defects, especially considering that the results of PES-PEH investigation exclude a significant density of Si-based self-compensating defects, such as Si-complexes or Si_O acceptors. Moreover, the slight but surprising decrease in the Hall density versus Φ_{SiH_4} despite the increase of incorporated Si, shown by Figures 1c and 5, would suggest that the formation of such additional defects should be favoured by increasing doping. In fact, such a decrease is neither attributable (i) to a reduction of the incorporation of Si impurities into the lattice for high Φ_{SiH_4} [11], (ii) nor a reduction of its occupancy of Ga sites [18], but rather to an increase in compensation or carrier trapping. Interestingly, the results of the TEM investigation proposed in Section 4.2 suggest that the Φ_{SiH_4} increase promotes the formation of APB shift-defects, highlighted in Figure 7. Since the density of such defects was found to increase with doping, one may assume a corresponding increase in the density of dangling bonds localized at the APB shift-defects, which could form acceptor complexes and/or trap carriers, enhancing the compensation, thus suggesting a peculiar doping-dependent compensation mechanism.

In this context, a comment on the role of the incorporated hydrogen (ERDA data) is appropriate. The detection of only one EPR spectrum at all temperatures ascribed to a Si-donor, with density comparable to the carrier concentration [12], combined with the evidence of Si-incorporation only into Ga sites [18], weakens the hypothesis of noticeable quantities of H_i or H_O shallow donors (see Section 2.3 for some details on H-related defects). Therefore, the main effect of hydrogen on the net donor concentration would result in the passivation of compensating acceptors by formation of acceptor-H complexes (e.g., $V_{Ga}H_n$). The formation energy and the transition levels of deep acceptors and several complexes with hydrogen in κ-Ga_2O_3 were calculated and reported in Ref. [19]. In conclusion, the incorporation of hydrogen is expected to enhance the net donor concentration in κ-Ga_2O_3 through partial passivation of acceptors, rather than generation of shallow levels.

5.4 | Applicability of Hall Effect Measurements in Case of VRH Transport

The use of Hall measurement data in the VRH transport regime is a very critical question, as discussed by Castner [16] and recalled in Section S1, because the signal cannot be explained in classical terms by the Lorentz force [38], rather as a quantum

interference effect [48, 49]. Therefore, it is crucial to compare the Hall density, derived from the usual transport formulas ($R_H = 1/ne$) and obtained in van der Pauw geometry, with the net donor densities provided by other experimental methods. In this contest, attention was paid to compare also variations of the measured densities with the silane flow, to corroborate the decreasing trend with Φ_{SiH_4} highlighted by Figures 1c and 5.

The sign of the Hall voltage in our samples resulted consistent with negatively charged carriers (according to Ref. [15]), in line with the Si incorporation in Ga sites [12, 18] and the similarity between the band structure of κ-Ga_2O_3 and the other polymorphs [13]. The *n*-type doping is also consistent with the rectifying behavior of heterojunctions based on Si-doped κ-Ga_2O_3 and a p-type SnO layer [20].

The comparison between *RT* transport data and capacitance–voltage (*C–V*) profiles carried out on the very same Si-doped layers [20] corroborated the agreement between *RT* Hall density and *n*-doping level. The *C–V* data were acquired in a range of frequencies (higher than 200 KHz) where the dissipation factor (*D*-factor) was lower than 0.5; no contribution from deep levels was detected in the whole frequency range. The *C–V* density resulted in the order of 10^{18} cm^{-3}, interpretable as the net density of shallow donors at the edge of the space charge region of a junction. In this framework, a source of uncertainty is the value of the static dielectric constant ε_s. In Ref. [20], $\varepsilon_s = 10.2$ has been assumed in analogy with β-Ga_2O_3; however, recent literature suggested higher values of ε_s between 15 and 32 for κ-Ga_2O_3 [19, 50]. Such uncertainty would be reflected in the *C–V* density estimation within a factor of 3.

In this work, the *RT* Hall density was instead compared with the density of EPR-detected $S = 1/2$ spins, which is expected to equal the net density of effective-mass donors [12]. The comparison was made as a function of Φ_{SiH_4}. Even in this case discrepancies have been observed [see Figure 6b], probably related to the different physical mechanisms generating the signals and the assumed approximations in the two experimental methods. Interestingly, both the sets of data exhibit an average decreasing trend versus Φ_{SiH_4}, superimposed to very similar relative variations; this supports the close correlation between the two sets of measures, as in the comparison of the data in Figure 6a. On the other hand, the absolute values of the EPR and Hall density data differ for a factor of about 4.

To explain this discrepancy, one can consider that the spin density was obtained from the analysis of the EPR spectra of electrons in the CB or IB using a reference sample with Curie-like paramagnetism. The uncertainty in the EPR spin concentration is estimated to be less than a factor of 2. Applying a correction of this magnitude shifts the spin density toward the *RT* Hall density, both reducing their discrepancy and better approaching the estimated critical density for the Mott transition, as consistent with the detection of motional narrowing effects in EPR linewidth [12]. The spin density is still lower than the Hall density, but the discrepancy becomes now comparable to that between *C–V* and Hall density data.

As concerns the most relevant source of uncertainty in the Hall density data carried out in the van der Pauw geometry, the presence of disorder represented by both rotational domains and APBs may introduce detrimental local inhomogeneities (see Ref. [51]). In addition, the measurement of Hall voltage can be affected by the finite dimension of electrical contacts [52], and, in the case of VRH transport, an unfavorable signal-to-noise ratio due to low mobility values.

A further, minor, critical parameter in this comparison could be the effective thickness of the layer where silicon atoms are incorporated as donors. In fact, a defective region was detected in the κ-Ga_2O_3 layers up to about 200 nm from the interface with the substrate in which the distribution of Si atoms is significantly different than the rest of the layer, due to the presence of pyramidal SiO_2 precipitates [11] (see Section 2.2). If such a region were assumed to be electrically inactive, the effective thickness of the doped films would be about 20% smaller, independently of the Φ_{SiH_4}. However, this could affect the evaluated densities in both electrical and EPR data.

Even considering these uncertainties, the comparison shown in Figure 6b is meaningful for the reliability of the Hall density data in the VRH regime, confirming (i) its absolute value within a factor of ≈2–3 at most, and (ii) its usual relationship with the carrier density, and, notably, (iii) its decreasing trend versus Φ_{SiH_4}. The similarity with EPR data also permits to exclude that the observed trend of the Hall density (and of the Hall mobility) versus Φ_{SiH_4} of Figure 4 is affected by other effects such as mixed conduction phenomenon.

Finally, because the decrease in the Hall density with Φ_{SiH_4} is confirmed, the reliability of the observed increase in mobility is also supported, as further discussed in Section 5.5.

5.5 | Temperature-Dependent Hall Data

The dependence on the silane flow observed for the density and mobility data in Figure 1 is also maintained at low temperatures, as Figures 4 and 5 show. The $\mu_H(T)$ curves of Figure 4a are always monotonically increasing, as expected for thermally activated transport, generally with a weaker dependence the higher their absolute values are. Interestingly, if reported in Mott plots (Figure 4b), to be consistent with the interpretation of the transport data proposed above, the mobility data roughly approach linear trends, in accordance with the trend: $\ln(\mu_H) \propto -\alpha(T_0/T)^{1/4}$, like predictions of percolation theory (Ref. [16] and references therein). Again, roughly *HT* and *LT* trends are evidenced as in the resistivity curves. Similar conclusions can be drawn for the Hall density data, which exhibit even more convincing linear behaviours in the Mott plots (Figure 5), especially in the *HT* range. In Figure 5, only the Hall density data for some selected samples are reported, which showed the least scattered trends. Figure 4b zooms in on the mobility data to match the density curves of Figure 5.

The *HT* linear trends in the Hall density Mott plots of Figure 4 have slopes s_n^{HT} in absolute value about one third than the corresponding ones s_ρ^{HT} of the resistivity Mott plots [see Table 2]. At low temperatures, the scattering of the data increases significantly and only a change in the dominant transport mechanism can be noticed, consistently with the overall picture of two *LT* and

TABLE 2 | Results of the analysis of the Hall density data versus temperature in a linear plot, after the approximation to Equation (2). m_n^{HT} is the slope (Figure 11). g_F^T is the density of the states in the *HT* range, ξ is the localization length. $n_H^{exp}(RT)$ is the experimental Hall density at RT. $N_S(RT) = g_F\, w_{opt}$ is the density of available sites at the temperature $T = 300$ K, giving a lower donor density estimation. The deviation of $N_S(RT)$ from $n_H^{exp}(RT)$ shows the self-consistency limit of the approach. The uncertainty in m_n^{HT} slopes is within 10%.

Sample n.	Φ_{SiH_4} sccm	m_n^{HT} ($cm^{-3}\,T^{-3/4}$)	ξ (nm)	g_F^{HT} (1/[eV cm^3])	N_S at *RT* (cm^{-3})	n_H^{exp}(RT) (cm^{-3})	$2 \times n_{spin}^{exp}$(RT) (cm^{-3})
507	12	1.98×10^{16}	4.22	1.6×10^{20}	2.85×10^{18}	3.45×10^{18}	1.92×10^{18}
506	15	1.14×10^{16}	6.29	1.14×10^{20}	1.65×10^{18}	2.35×10^{18}	1.92×10^{18}
508	15	1.33×10^{16}	7.06	1.57×10^{20}	1.19×10^{18}	2.84×10^{18}	1.80×10^{18}
510	17.5	1.09×10^{16}	5.71	9.72×10^{19}	1.57×10^{18}	1.72×10^{18}	1.2×10^{18}

HT VRH trends, with the tendency for a lower s_n^{LT} slope with respect to s_n^{HT}. In any case, both these slopes are weaker than those predicted by the percolation approach. Therefore, the trend of mobility with temperature is stronger than that proposed in Ref. [16], where the expected trends of Hall density and Hall mobility are $\ln(n_H) \propto -\frac{5}{8}(T_0/T)^{1/4}$ and $\ln(\mu_H) \propto -\frac{3}{8}(T_0/T)^{1/4}$, respectively, as recalled in Section S1. However, Koon and Castner observed that the γ coefficient in the Hall density law, written as: $\ln(n_H) \propto -\gamma(T_0/T)^{1/4}$, tends to increase by approaching the MIT (and to decrease with the applied magnetic field); therefore, it can be supposed that the carrier concentration of our samples is farther from the MIT with respect to the case of their study [16, 53]. It is also reasonable to expect that the α and γ coefficients, with $\alpha + \gamma = 1$ consistently with Mott's law for resistivity as predicted by the percolation approach, can depend on the details of the structural disorder, for example, the results obtained in this work may be influenced by rotational domains. It should be also stressed that, unlike the measures cited in Ref. [16], in our samples VRH transport is observed in a wide range of temperatures at least up to *RT*, a condition already pointed out for conductivity in other disordered wide-bandgap semiconductors [36, 54], and here also extended to Hall density and mobility data. We highlight these intriguing, even if qualitative, results versus temperature, rarely reported by literature, which are consistent with the VRH transport properties.

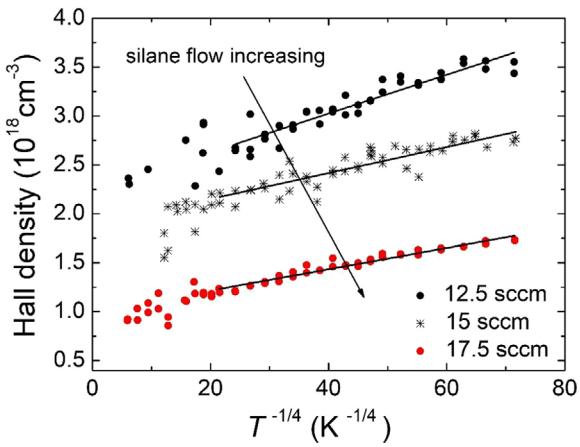

FIGURE 11 | Temperature dependence of the Hall density versus $T^{3/4}$ for the doped samples of Figure 5. Symbols: experimental data (see the legend in the picture); continuous lines: linear best fits (fitted slopes are reported in Table 2).

5.6 | Phenomenological Description of n(*T*) and Comments on ξ

A phenomenological definition of carrier density is proposed here, which is qualitatively consistent with the temperature dependence expected from the percolation approach to VRH transport, under the assumptions of three-site clusters and low-field, low-temperature limits. The aim of the calculation is to speculate on the value of the parameter ξ, which enters in the VRH analysis of the experimental Hall density data, and the variation of ξ with Φ_{SiH_4}.

In this phenomenological approach the carrier density $n(T)$ is assumed equal to the product $n_T(T)P_w(T)$, where $n_T(T)$ is the density of occupied sites in the $w_{opt}(T)$ band at a given temperature T, and $P_w(T)$ is the probability of a thermally activated hop of a carrier into another site, taking w_{opt} as the activation energy. Then, the density of occupied donors is set equal to the density of energy states lying in a band of width w_{opt} times the density of states g_F, then: $n_T \approx g_F w_{opt}$, so that:

$$n\ (T) = n_T \exp\left(-w_{opt}/\left(K_B T\right)\right) \tag{2}$$

n_T roughly depends on $T^{3/4}$, whereas $w_{opt}/(K_B T) = (1/4)\,(T_0/T)^{1/4}$. Compensation effects are expected to be included in $g_F w_{opt}$, according to Ref. [16]. In the following, the discussion of the $n_H(T)$ data versus Φ_{SiH_4} will be focused on the *HT*-range of VRH transport, which shows a better-defined temperature dependence (see Figure 5).

The interest for this definition lies in its ability to justify both the detection of quite linear trends when the experimental $n_H(T)$ data are reported on a linear scale versus $T^{3/4}$, as Figure 11 shows for selected samples, and also the *HT* linear trends in Mott plots of Figure 5. The possibility of this double analysis of the data is due to the weak dependence on the temperature of $n(T)$ and of both the pre-exponential and exponential factors.

We observe that for all the samples here considered, it always happens that $w_{opt}/K_B T \approx 0.5$ in *HT* range (i.e., $RT \geq T > 100\ K$). Then, the exponential term does not deviate too much from this value, observing that $\exp(-w_{opt}/(K_B T)) \approx 1 - w_{opt}/(K_B T) \approx 0.5$. In this way $n(T) \approx 0.5 g_F w_{opt}$ which is be expected to approach

a $T^{3/4}$ temperature dependence, as experimentally observed, and the slope can be interpreted as $m_n^{HT} = 0.5(C/(4\xi^3))(1/T_0)^{3/4}$.

This conclusion does not contrast with the Mott plot of Figure 5, because it can be assumed that the weak dependence on temperature of the pre-exponential factor only slightly influences the slope of this plot, whose experimental value approaches $(1/3)s_\rho^{HT}$, that is, $s_n^{HT} \approx (1/3)(T_0/T)^{1/4}$, instead of $(1/4)(T_0/T)^{1/4}$ predicted by Equation (2) for a constant pre-exponential factor.

Using the T_0 data obtained from the *HT* linear fit of the resistivity Mott plot in m_n^{HT} and adjusting the ξ-value to fit theoretical to experimental slopes, localization length values of a few nm (5–7 nm) were found to be appropriate for all the samples [15, 36], with a tendency to increase with Φ_{SiH_4}, as appears from Table 2. Here the data of samples grown at silane flows of 7.5 and 10 were not reported because the scattering of the data makes the linear fit of their data difficult. Although roughly obtained, this result agrees with the supposition that the localization length has similar values for all the investigated samples, only weakly increasing with the silane flow, that is, in line with the above comments on g_F. This value is slightly larger than values assumed in literature for VRH transport, of the order of the nm (about 1–3 nm) [36, 54].

Consistent with the Mott theory, ξ is higher than the Bohr radius evaluated for a hydrogenic impurity in κ-Ga_2O_3, which is equal to 1.8 nm if an effective mass 0.3 m_e, and a dielectric constant $\varepsilon_s = 10.2$ are considered (the comparison would become more critical for higher values of ε_s, although again $\xi \geq a_B$). The g_F^{HT} values that result from this analysis are weakly dependent on the silane flow with a tendency to decrease, as Figure 2S in Supporting Information suggests, whereas ξ slightly tends to increase. The estimated N_S at *RT* are compared in Table 2 with the experimental *RT* values of the Hall density. Notice that, according to the definition of $N_S = g_F\, w_{opt}$, this quantity is derived at any temperature from the slopes of the linear Mott plots for resistivity ($T_0^{1/4}$), indicating a self-consistency of the electrical data, and supporting its assumption as an underestimation of net donor density.

It is worth noting that as *HT*-VRH is attributed to hopping between donor clusters, then in principle $g_F w_{opt}$ is related to cluster density. However, the difference between the density of donors and the density of donor clusters could become a factor of the order of unity and be comparable to the accuracy of the Hall data in the VRH regime.

5.7 | Structural Defects and Their Effects on Carrier Mobility

The purpose of this section is to justify the increase of the Hall mobility with Φ_{SiH_4}, even if the compensation and the density of incorporated silicon increase.

In undoped κ-Ga_2O_3 samples, where the mean domain size is 5–20 nm, domain boundaries play a crucial role in limiting the in-plane conductivity, as suggested by the difference of at least one order of magnitude between in-plane and out-of-plane resistivity [11]. The study of transport was found to be temperature-activated, although the conduction mechanism was not clearly identified because of the restricted temperature range where electrical measurements could be carried out (see Ref. [13] or Figure 3a). In doped samples, however, $\rho(T)$ data were found to be consistent with VRH mechanisms for every used Φ_{SiH_4}, despite the demonstrated enlargement of domains up to about one order of magnitude in the range $5 \leq \Phi_{SiH_4} \leq 17.5$ sccm [11]. Such domain expansion with larger Φ_{SiH_4} resulted in the reduction of the full width at half maximum of ω-scans (rocking curve) of the (004) peak in XRD, in reduction of phonon mean free path and phonons lifetimes in Raman investigation, and in appreciable improvement of the in-plane mobility in electrical measurement. In this experimental framework, the in-plane mobility increase (Figure 1b and Figure 4) can be attributed to the beneficial effect of the higher crystalline quality (less boundaries due to the domain expansion), however contrasted by the dense formation of APBs, which are expected to hinder carrier transport.

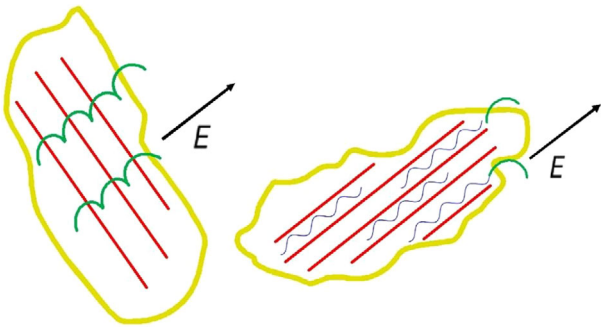

FIGURE 12 | Simplified picture of the transport in the two limit conditions of electric field E (black arrows) perpendicular or parallel to the planar APBs, with carriers moving respectively (i) crossing the APB and the domain boundaries with low-mobility transport (green hops) or (ii) along the planar APBs (blue drawings indicating higher mobility hopping transport). For any direction of E with respect to the crystallographic *b*-directions in each domain, carrier transport can take place in part crossing defective boundaries (low mobility transport) and in part along the volume between them (high mobility transport), resulting in an in-plane anisotropic transport. The contribution of the high mobility conduction increases with the larger linear dimension of the domains, resulting in an enhanced mobility.

As commented above, the APBs (Figure 7) are supposed to play a critical role on the transport properties of κ-Ga_2O_3 as they may act as carrier traps and/or self-compensation factors. In particular, they are sites of APB shift-defects, whose density was found to be doping-dependent; therefore, with increasing dopant concentration, the associated point defects and dangling bonds may also give rise to additional acceptor complexes (or traps), triggering self-compensation effects. Besides explaining the decrease in carrier density with increasing Φ_{SiH_4} (Figure 1c and Figure 6b), spatial charge and possibly depletion regions around APSs may hinder charge transport across them. Therefore, due to their preferential orientation along the *b*-direction of the orthorhombic cell, they may be expected to induce anisotropic transport within the single domain. However, due to the rotational nature of domains, anyway a mobility increasing with Φ_{SiH_4} can be expected. This picture is represented in Figure 12 by a simple

sketch. Given the uniform distribution of extrinsic Si reported in Ref. [11], it is possible that in the volume between adjacent planar APB-defects the carriers move with higher mobility, consistently with a VRH between donor clusters, according to Ref. [12] and a quite delocalized wavefunction on short distances, as detected by EPR investigation. Differently, carrier transport across extended defective APB planes or domain boundaries is strongly hindered.

Fixed the orientation of an applied electric field, the in-plane electrical transport in each domain takes place with low mobility orthogonally to the APB boundaries, whereas a higher mobility is allowed along the *b*-direction of the domain. In a simple sketch (Figure 12), this can be described by assuming a fraction of domains that have their *b*-axis predominantly aligned with the field, where carriers can move with higher mobility for long traits within the volume delimited by adjacent APB defects, whereas in the other domains low-mobility hopping transport dominates because carriers must traverse several extended defective regions and domain boundaries to be drifted. Anisotropy effects on in-plane transport within a domain, induced by the planar APB defects therein, are magnified by domain enlargement. Indeed, the high-mobility conduction along the *b*-direction gains greater relevance, inducing an increase in the total in-plane mobility of the layer, as observed experimentally, yet leaving the hopping mechanism of transport (VRH) overall dominant, consistent with the whole picture of transport in these layers.

6 | Conclusions

The temperature dependence of resistivity, Hall density, Hall mobility, and EPR linewidth in Si-doped κ-Ga_2O_3 layers grown by MOVPE was investigated as a function of Si doping. The trends were found to be consistent with the VRH transport mechanism over the entire Si-doping range. Two different VRH regimes, at low and high temperatures, were evidenced by resistivity and EPR measurements, as in previous literature: the two regimes resulted here appreciable also in the Hall data, showing trends in agreement with the expectations of the percolation theory for VRH transport. The resistivity curves were analyzed in the light of the Mott theory, and the hopping parameters relevant for this conduction mechanism were derived— the density of states at the Fermi energy g_F, the optimum energy w_{opt}, the optimum radius R_{opt} and the localization length ξ—to demonstrate the overall coherence of the interpretative framework.

The evolution of the resistivity data and EPR results with increasing silane flow indicated that the electronic system is approaching the MIT transition for about $\Phi_{SiH_4} > 5$ sccm but never crosses it. Moreover, the density of incorporated Si in Ga-sites, without evidence of precipitates, is two orders of magnitude higher than the Hall density, indicating a very high compensation level, higher than 90%. This is consistent with a Fermi level position intersecting the deeper localized states of a CB band tail that incorporates the Si_{Ga} donor levels, almost completely emptied by the very high compensation for any Φ_{SiH_4}. Then, the physical system falls at the insulating side of MIT, the transition to metal conduction being inhibited by high compensation. Self-consistently, a nearly constant localization length ξ was here evaluated thanks to a phenomenological model for Hall density. This picture also agrees with other findings: (i) a rough estimate of the IB energy position, from the resistivity data, placing it a few tens of meV below the CB minimum, comparable to the energy of hydrogenic donor states, unambiguously identified as substitutional Si to Ga. (ii) DFT prediction of effective-mass states for Si in all the Ga-sites, with preferential occupancy of the tetrahedral site, in agreement with EPR and previous PES-PEH results. (iii) Since HR-TEM indicates a spatially uniform dopant distribution in the conductive layer, the four Si_{Ga} donor states are broadened into an IB by high doping and disorder, with an expected width of each contribution depending on its relative density.

Regarding disorder and compensation, which play such a disruptive role in the electronic properties of the material, results were obtained from TEM investigations. The formation of APB planes within the rotational domains, oriented along the *b*-axis of the orthorhombic cell, was confirmed. The increased mobility with higher Φ_{SiH_4} was shown to be compatible with the APBs' presence, through a phenomenological model. However, in doped layers, TEM images evidenced additional defects located at APBs, which we called APB shift-defects, whose density was here demonstrated to increase with increasing Φ_{SiH_4} and may justify a doping-dependent compensation level. Dangling bonds or additional point defects are probably triggered by such APB-related defects, which in turn may further enhance the compensation, however given by acceptor defects like V_{Ga} and split vacancies. All these prevent the achievement of high conductivity despite heavy Si-doping. In this context, it was also concluded that hydrogen from water, carrier gas, and silane flows, incorporated in the layers in large amounts, contributes to the transport properties mainly by passivating intrinsic deep acceptors (e.g., simple or split V_{Ga}), rather than behaving as shallow donors (co-doping).

The net doping level of the samples was evaluated by critically comparing VRH–Hall density with the results of EPR investigation on the same samples, and previous *C*–*V* measurements on similar Si-doped samples. Evaluations of the DOS at the Fermi level, obtained from the Mott theory, were consistent with the experimental densities. The demonstrated equivalence between Hall density and carrier density proves the applicability of Hall voltage in VRH transport analysis and justifies the interpretation of the Hall coefficient as the inverse of the charge carrier density (hopping carriers) and the elementary charge *e*. The coupling of EPR and transport measurements was then confirmed to be a good strategy for investigating the electronic properties of such systems. The two investigations made on the same set of samples were crucial to demonstrate that the carrier density decreased for increasing silane flow, hence the occurrence of doping-dependent compensation at least in the investigated doping range.

Together with the related literature, this work sheds light on the active conduction mechanism in silicon-doped κ-Ga_2O_3 layers deposited by MOVPE on sapphire, rarely discussed in the literature, and allows to clarify the extrinsic effects that have an impact on the electronic properties of the material. The in-depth study of hopping-driven conduction near the metal-insulator transition, supported by multiple characterization techniques, allowed us to shed light on the compensation/self-compensation phenomena in Si-doped κ-Ga_2O_3. The critical comparison of Hall density data and EPR spin density is a key aspect of the present treatment as it allowed to assess the applicability of Hall voltage in the analysis

of VRH transport. This approach is of methodological relevance and can profitably be applied to other defective material systems.

Acknowledgements

The authors would like to thank Dr. Matteo Bosi and Luca Seravalli for epitaxial layer deposition as well as Salvatore Vantaggio for technical assistance. The MOVPE epitaxial growth of Ga_2O_3 is supported by the Italian National Recovery and Resilience Plan (PNRR) funded by NextGenerationEU, Mission 4, Component 2, Project "Ecosystem for Sustainable Transition in Emilia-Romagna – (Ecosister) – Code ECS00000033". This research was granted by the University of Parma through the action Bando di Ateneo 2021 per la ricerca co-funded by MUR-Italian Ministry of Universities and Research – D.M. 737/2021 – PNR – PNRR – NextGenerationEU, project "MUR_DM737_A_MAFI_PARISINI DM 737 25.06.2021 – Ga2O3-based diodes for power electronics". Project no. NKFIH ADVANCED 152987 has been implemented with the support provided by the Ministry of Culture and Innovation of Hungary from the National Research, Development and Innovation Fund (NRDIF). I. Cora thanks the János Bolyai Research Scholarship of the Hungarian Academy of Sciences for its support. Finally, the authors acknowledge the French EMIR-A network through proposal 24-02-15 for access to the SAFIR platform for ERDA measurements.

Open access publishing facilitated by Universita degli Studi di Parma, as part of the Wiley - CRUI-CARE agreement.

Conflicts of Interest

The authors declare no conflicts of interest.

Data Availability Statement

Data will be provided upon request.

References

1. S. Pearton, F. Ren, and M. Mastro, ed., *Gallium Oxide- Technology, Devices and Applications*, (Elsevier, 2019), ISBN: 9780128145210.

2. M. Higashiwaki and S. Fujita, ed., *Gallium Oxide: Materials Properties, Crystal Growth, and Devices* (Springer Nature, 2020), https://doi.org/10.1007/978-3-030-37153-1, ISBN: 978-3-030-37152-4.

3. B. R. Tak, S. Kumar, A. K. Kapoor, et al., "Recent Advances in the Growth of Gallium Oxide Thin Films Employing Various Growth Techniques - A Review," *Journal of Physics D: Applied Physics* 54 (2021): 453002, https://doi.org/10.1088/1361-6463/ac1af2.

4. I. Cora, F. Mezzadri, F. Boschi, et al., "The Real Structure of ε-Ga_2O_3 and Its Relation to the κ-Phase," *CrystEngComm* 19 (2017): 1509–1516, https://doi.org/10.1039/c7ce00123a.

5. P. Mazzolini, A. Falkenstein, C. Wouters, et al., "Substrate-Orientation Dependence of **β**-Ga2O3 (100), (010), (001) Homoepitaxy by Indium-Mediated Metal-Exchange Catalyzed Molecular Beam Epitaxy (MEXCAT-MBE)," *APL Materials* 8 (2020): 011107, https://doi.org/10.1063/1.5135772.

6. A. Fiedler, R. Schewski, M. Baldini, et al., "Influence of Incoherent Twin Boundaries on the Electrical Properties of β-Ga_2O_3 Layers Homoepitaxially Grown by Metal-Organic Vapor Phase Epitaxy," *Journal of Applied Physics* 122 (2017): 165701, https://doi.org/10.1063/1.4993748.

7. M. Bosi, P. Mazzolini, L. Seravalli, and R. Fornari, "Ga_2O_3 Polymorphs: Tailoring the Epitaxial Growth Conditions," *Journal of Materials Chemistry C* 8 (2020): 10975–10992, https://pubs.rsc.org/en/content/articlelanding/2020/TC/D0TC02743J.

8. R. Fornari, M. Pavesi, V. Montedoro, et al., "Thermal Stability of ε-Ga_2O_3 Polymorph," *Acta Materialia* 140 (2017): 411–416, https://doi.org/10.1016/j.actamat.2017.08.062.

9. F. Mezzadri, G. Calestani, F. Boschi, D. Delmonte, M. Bosi, and R. Fornari, "Crystal Structure and Ferroelectric Properties of ε-ga_2O_3 Films Grown on (0001)-Sapphire," *Inorganic Chemistry* 55 (2016): 12079–12084, https://pubs.acs.org/doi/10.1021/acs.inorgchem.6b02244.

10. H. Nishinaka, O. Ueda, D. Tahara, et al., "Single-Domain and Atomically Flat Surface of κ-ga_2O_3 Thin Films on FZ-Grown ε-$GaFeO_3$ Substrates via Step-Flow Growth Mode," *ACS Omega* 5 (2020): 29585–29592, https://doi.org/10.1021/acsomega.0c04634.

11. P. Mazzolini, Z. Fogarassy, A. Parisini, et al., "Silane-Mediated Expansion of Domains in Si-Doped κ-Ga_2O_3 Epitaxy and Its Impact on the in-Plane Electronic Conduction," *Advanced Functional Materials* 33 (2022): 2207821, https://doi.org/10.1002/adfm.202207821.

12. H. J. von Bardeleben, J. L. Cantin, A. Parisini, A. Bosio, and R. Fornari, "Conduction Mechanism and Shallow Donor Properties in Silicon Doped ε-Ga_2O_3 Thin Films: An Electron Paramagnetic Resonance Study," *Physical Review Materials* 3 (2019): 084601, https://doi.org/10.1103/PhysRevMaterials.3.084601.

13. A. Parisini, A. Bosio, H. J. von Bardeleben, et al., "Deep and Shallow Electronic States Associated to Doping, Contamination and Intrinsic Defects in ε-Ga_2O_3 Epilayers," *Materials Science in Semiconductor Processing* 138 (2022): 106307, https://doi.org/10.1016/j.mssp.2021.106307.

14. O. F. Vyvenko, S. V. Shapenkov, E. V. Ubyivovk, et al., "Twin Domain and Antiphase Boundaries in Microcrystals of κ-Phase Ga_2O_3," *Materialia* 32 (2023): 101942, https://doi.org/10.1016/j.mtla.2023.101942.

15. A. Parisini, A. Bosio, V. Montedoro, et al., "Si and Sn Doping of ε-Ga_2O_3 Layers," *APL Materials* 7 (2019): 031114, https://doi.org/10.1063/1.5050982.

16. T. G. Castner, "Hopping Conduction in the Critical Regime Approaching the Metal-Insulator Transition," in *Hopping Transport in Solids*, ed. M. Pollak and B. Shklovskii (Wiley, 1991), 1–49, https://doi.org/10.1016/c2009-0-12721-6.

17. P. P. Altermatt, A. Schenk, and G. Heiser, "A Simulation Model for the Density of States and for Incomplete Ionization in Crystalline Silicon. I. Establishing the Model in Si:P," *Journal of Applied Physics* 100 (2006): 113714, https://doi.org/10.1063/1.2386934.

18. Y. Tsai, Y. Hashimoto, Z. X. Sun, et al., "Photoelectron Holographic Study for Atomic Site Occupancy for Si Dopants in Si-Doped κ-Ga_2O_3(001)," *Nano Letters* 24 (2024): 3978–3985, https://doi.org/10.1021/acs.nanolett.4c00482.

19. P. Mazzolini, J. B. Varley, A. Parisini, et al., "Engineering Shallow and Deep Level Defects in κ-Ga_2O_3 Thin Films: Comparing Metal-Organic Vapour Phase Epitaxy to Molecular Beam Epitaxy and the Effect of Annealing Treatments," *Materials Today Physics* 45 (2024): 101463, https://doi.org/10.1016/j.mtphys.2024.101463.

20. P. R. Kalvani, A. Parisini, G. Sozzi, et al., "Interfacial Properties of SnO/κ-Ga_2O_3 p-n Heterojunction: A Case of Subsurface Doping Density Reduction via Thermal Treatment in κ-Ga_2O_3," *ACS Applied Materials and Interfaces* 15 (2023): 45997–46009, https://doi.org/10.1021/acsami.3c08841.

21. A. Bosio, C. Borelli, A. Parisini, M. Pavesi, S. Vantaggio, and R. Fornari, "A Metal-Oxide Contact to ε-Ga_2O_3 Epitaxial Films and Relevant Conduction Mechanism," *ECS Journal of Solid State Science and Technology* 9 (2020): 055002, https://doi.org/10.1149/2162-8777/ab8f37.

22. S. Seacat, J. L. Lyons, and H. Peelaers, "Properties of Orthorhombic Ga_2O_3 Alloyed With In_2O_3 and Al_2O_3," *Applied Physics Letters* 119 (2021): 042104, https://doi.org/10.1063/5.0060801.

23. T. Gake, Y. Kumagai, and F. Oba, "First-Principles Study of Self-Trapped Holes and Acceptor Impurities in Ga_2O_3 Polymorphs," *Physical Review Materials* 3 (2019): 044603, https://doi.org/10.1103/PhysRevMaterials.3.044603.

24. G. Kresse and J. Furthmüller, "Efficient Iterative Schemes for Ab Initio Total-energy Calculations Using a Plane-wave Basis Set," *Physical Review B* 54 (1996): 11169, https://doi.org/10.1103/PhysRevB.54.11169.

25. G. Kresse and D. Joubert, "From Ultrasoft Pseudopotentials to the Projector Augmented-Wave Method," *Physical Review B* 59 (1999): 1758, https://doi.org/10.1103/PhysRevB.59.1758.

26. J. Heyd, G. E. Scuseria, and M. Ernzerhof, "Hybrid Functionals Based on a Screened Coulomb Potential," *Journal of Chemical Physics* 118 (2003): 8207–8215, https://doi.org/10.1063/1.1564060.

27. F. Ricci, F. Boschi, A. Baraldi, et al., "Theoretical and Experimental Investigation of Optical Absorption Anisotropy in β-Ga_2O_3," *Journal of Physics: Condensed Matter* 28 (2016): 224005, https://doi.org/10.1088/0953-8984/28/22/224005.

28. B. I. Shklovskii and A. L. Efros, "Softcover Reprint of the Original 1st Edition 1984," in *Electronic Properties of Doped Semiconductors*, ed. V. B. Shklovskii and A. L. Ėfros (Springer-Verlag Berlin Heidelberg GmbH, 2013), ISBN: 3-540-12995-2.

29. N. F. Mott, *Metal-Insulator Transitions*, 2nd ed. (Taylor and Francis Ltd, 1990), ISBN: 13 9780850667837.

30. C. Freysoldt, J. Neugebauer, and C. G. Van de Walle, "Fully Ab Initio Finite-Size Corrections for Charged-Defect Supercell Calculations," *Physical Review Letters* 102 (2009): 016402, https://doi.org/10.1103/PhysRevLett.102.016402.

31. Y. Kumagai, N. Tsunoda, A. Takahashi, and F. Oba, "Insights Into Oxygen Vacancies From High-Throughput First-Principles Calculations," *Physical Review Materials* 5 (2021): 123803, https://doi.org/10.1103/PhysRevMaterials.5.123803.

32. J. B. Varley, J. R. Weber, A. Janotti, and C. G. Van de Walle, "Oxygen Vacancies and Donor Impurities in β-Ga_2O_3," *Applied Physics and Letters* 97 (2010): 142106, https://doi.org/10.1063/1.3499306.

33. A. Shokri, Y. Melikhov, Y. Syryanyy, and I. N. Demchenko, "Point Defects in Silicon-Doped β-Ga_2O_3: Hybrid-DFT Calculations," *ACS Omega* 8 (2023): 43732–43738, https://doi.org/10.1021/acsomega.3c05557.

34. R. M. Hill, "On the Observation of Variable Rand Hopping," *Physica Status Solidi A* 35 (1976): K29–K34, https://doi.org/10.1002/pssa.2210350151.

35. C. Chuang, R. K. Puddy, H.-D. Lin, S.-T. Lo, T.-M. Chen, C. G. Smith, and C.-T. Liang, "Experimental Evidence for Efros–Shklovskii Variable Range Hopping in Hydrogenated Graphene," *Solid State Communications* 152 (2012): 905–908, https://doi.org/10.1016/j.ssc.2012.02.002.

36. A. Parisini, A. Parisini, and R. Nipoti, "Size Effect on High Temperature Variable Range Hopping in Al^+Implanted 4H-SiC," *Journal of Physics: Condensed Matter* 29 (2017): 035703, https://doi.org/10.1088/1361-648X/29/3/035703.

37. N. Mott, "Impurity Band Conduction. Experiment and Theory – The Metal-Insulator Transition in an Impurity Band," *Journal de Physique Colloques* 37, no. C4 (1976): C4301–C4306, https://doi.org/10.1051/jphyscol:1976453.

38. N. F. Mott and E. A. Davis, *Electronic Processes in Non-Crystalline Materials* (Clarendon Press Oxford, 1971), ISBN: 13 978-0198512592.

39. M. Guc, R. Caballero, K. G. Lisunov, et al., "Disorder and Variable-Range Hopping Conductivity in Cu_2ZnSnS_4Thin Films Prepared by Flash Evaporation and Post-Thermal Treatment," *Journal of Alloys and Compounds* 596 (2014): 140–144, https://doi.org/10.1016/j.jallcom.2014.01.177.

40. K. G. Lisunov, M. Guc, S. Levcenko, et al., "Energy Spectrum of Near-Edge Holes and Conduction Mechanisms in $Cu_2ZnSiSe_4$Single Crystals," *Journal of Alloys and Compounds* 580 (2013): 481–486, https://doi.org/10.1016/j.jallcom.2013.06.156.

41. K. G. Lisunov, B. Raquet, H. Rakoto, et al., "Variable-Range Hopping Conductivity in Thin Film of the Ladder Compound $[Ca_{1+\delta}Cu_2O_3]_4$," *Journal of Applied Physics* 94 (2003): 5912–5917, https://doi.org/10.1063/1.1603961.

42. K. G. Lisunov, E. K. Arushanov, C. Kloc, U. Malan, and E. Bucher, "Hopping Conductivity in p-Type β-$FeSi_2$," *Physica Status Solidi B: Basic Solid State Physics* 195 (1996): 227–236, https://doi.org/10.1002/pssb.2221950125.

43. K. G. Lisunov, M. Guc, A. Nateprov, S. Levcenko, V. Tezlevan, and E. Arushanov, "Features of the Acceptor Band and Properties of Localized Carriers From Studies of the Variable-Range Hopping Conduction in Single Crystals of p-Cu_2ZnSnS_4," *Solar Energy Materials & Solar Cells* 112 (2013): 127–133, https://doi.org/10.1016/j.solmat.2013.01.027.

44. A. Bosio, A. Parisini, A. Lamperti, et al., "n-Type Doping of ε-Ga_2O_3 Epilayers by High-Temperature Tin Diffusion," *Acta Materialia* 210 (2021): 116848, https://doi.org/10.1016/j.actamat.2021.116848.

45. U. Thomanschefsky and D. F. Holcomb, "Metal-Insulator Transition in the Compensated Semiconductor Si: (P,B)," *Physical Review B* 45 (1992): 13356, https://doi.org/10.1103/PhysRevB.45.13356.

46. P. P. Poduval and S. D. Sarma, "Anderson Localization in Doped Semiconductors," *Physical Review B* 107 (2023): 174204, https://doi.org/10.1103/PhysRevB.107.174204.

47. A. Karjalainen, I. Makkonen, J. Etula, et al., "Split Ga Vacancies in n-Type and Semi-Insulating β-Ga_2O_3Single Crystals," *Applied Physics Letters* 118 (2021): 072104, https://doi.org/10.1063/5.0033930.

48. T. Holstein, "Hall Effect in Impurity Conduction," *Physical Review* 124 (1961): 1329, https://doi.org/10.1103/PhysRev.124.1329.

49. M. S. Reistad, "*Monte Carlo Simulations of Hall Effect in Variable Range Hopping Systems*" (Master's Thesis, University of Oslo, 2019).

50. S. Yusa, D. Oka, and T. Fukumura, "High-κ Dielectric ε-Ga_2O_3 Stabilized in a Transparent Heteroepitaxial Structure Grown by Mist CVD at Atmospheric Pressure," *CrystEngComm* 22 (2020): 381–385, https://doi.org/10.1039/c9ce01532a.

51. T. Matsumura and Y. Sato, "A Theoretical Study on Van Der Pauw Measurement Values of Inhomogeneous Compound Semiconductor Thin Films," *Journal of Modern Physics* 1 (2010): 340–347, https://doi.org/10.4236/jmp.2010.15048.

52. R. Chwang, B. J. Smith, and C. R. Crowell, "Contact Size Effects on the van der Pauw Method for Resistivity and Hall Coefficient Measurement," *Solid-State Electron* 17 (1974): 1217–1227, https://doi.org/10.1016/0038-1101(74)90001-X.

53. D. W. Koon and T. G. Castner, "Variable-Range Hopping and the Hall Coefficient in Si: As," *Solid State Communications* 64 (1987): 11–14, https://doi.org/10.1016/0038-1098(87)90509-6.

54. A. Yildiz, S. B. Lisesivdin, M. Kasap, and D. Mardare, "High Temperature Variable-Range Hopping Conductivity in Undoped TiO_2Thin Film," *Optoelectronics and Advanced Materials – Rapid Communications* 1 (2007): 531–533.

Supporting Information

Additional supporting information can be found online in the Supporting Information section.

Supporting File: aelm70510-sup-0001-SuppMat.docx.